DESIGN AND PROTOTYPING OF SUB-MILLIMETER-PERIOD UNDULATORS FOR FREE ELECTRON LASER

by

DERYA BERKIN GÜREL

Submitted to the Graduate School of Engineering and Natural Sciences

in partial fulfillment of

the requirements for the degree of Master of Science

Sabancı University

July 2021

DESIGN AND PROTOTYPING OF SUB-MILLIMETER-PERIOD UNDULATORS FOR FREE ELECTRON LASER

APPROVED BY:

DATE OF APPROVAL: 14/July/2021

DESIGN AND PROTOTYPING OF SUB MILLIMETER-PERIOD UNDULATORS FOR FREE ELECTRON LASER

DERYA BERKİN GÜREL

Materials Science and Nanoengineering, M.Sc. Thesis, 2021

Thesis Advisor: Prof. Dr. Burç Mısırlıoğlu

Co Adviser: Assoc. Prof. Dr. Ozan Akdoğan

Keywords: FePt, thin films, undulator, free-electron lasers, NdFeB, micromagnets, lithography, sputtering

ABSTRACT

The invention of the optical microscope in the 17th century shed light on the world of microorganisms, and later on, the invention of electron microscopes in 1931 opens up the world of structures in sub-nanometer dimensions. However, another but more powerful tool, Free Electron Laser (FEL), was invented in 1971 by John Madey. FEL shed light on a world, which is at the same time ultra-small (below 100 nm) and ultra-fast (down to fs), such as the hydrogen transfer time of the molecules (~1 ns), the spin precession time (~10 ps) and computing time (~1 ns). In a typical FEL, a beam of electrons is accelerated to almost the speed of light in an electron accelerator. E-beam then passes through an undulator; an insertion device consists of two parallel arrays of magnets with alternating polarity, facing each other with an air gap in between. Due to the alternating pattern of the magnetic field, electrons follow a sinusoidal path instead of going straight, which radiates energy. A Free Electron Laser generates tunable, coherent, high-power radiation, currently spanning wavelengths from millimeter to x-ray (XFEL).

One of the critical parameters of the XFEL is the undulator period which has a direct effect on the x-ray radiation. The current state of the art of XFEL'S; LCLS/SLAC uses an undulator period of 3 cm and creates an output radiation wavelength down to 1.5 A using an e-beam with the energy of ~14 GeV. However, this kind of high-energy e-beam could only be generated on gigantic accelerator facilities. Reducing the undulator period from 3 cm to 300 μm (short-period) would reduce the required e-beam energy to 1.4 GeV. Consequently, more compact e-beam sources could be used and make XFELs readily available for special applications. In a different perspective, short-period undulators would generate higher energy radiation when coupled with high-energy

electron accelerators, such as gamma rays, which would pave the way to discoveries in Science.

In this study, sub-millimeter-period Undulators will be designed and prototyped. Micron size magnets will be synthesized by using e-beam evaporation, triode sputtering, photo, and e-beam lithography. The produced micro magnets will be assembled into an undulator after rigorous modeling. Also, advanced synthesized micro-magnets could be used as the building blocks of the next generation of magnetic micro-tools. The project's ultimate goal would be testing the undulator in a running XFEL.

SERBEST ELEKTRON LAZERİ İÇİN MİLİM ALTİ PERIYOTLU SALINDIRICI TASARIM VE ÜRETİMİ

DERYA BERKİN GÜREL

Malzeme Bilimi ve Nano Mühendislik, Yüksek Lisans Tezi, 2021

Tez Danışmanı: Prof. Dr. Burç Mısırlıoğlu

Eş Danışman: Doç. Dr. Ozan Akdoğan

Anahtar Kelimeler: FePt, ince film, undulatör, serbest elektron lazeri, NdFeB, mikro mıknatıs, litografi, sputtering

ÖZET

17. yüzyılda optik mikroskopun icadı, mikroorganizmanın dünyasına ışık tutmuştur ve daha sonra 1931'de elektron mikroskoplarının icadı ile nanometre ve daha küçük boyutlardaki yapıların dünyası gözler önüne serilmiştir. Daha güçlü bir görüntüleme cihazı olarak Serbest Elektron Lazeri (SEL), 1971'de John Madey tarafından icat edildi. SEL, aynı anda hem ultra-küçük (100 nm'nin altında) ve hem de ultra-hızlı (fs'ye kadar) bir dünyanın görüntülenmesini sağlamıştır. Moleküllerin hidrojen transfer süresi (~ 1 ns), spinlerin manyetik alan altında dönme süresi (~ 10 ps) ve bilgisayardaki hesaplama süresi (~ 1 ns) ultra hızla gelişen olaylara örnek olarak verilebilir. Tipik bir SEL'de elektron demeti, elektron hızlandırıcısında ışık hızına yakın hızlara ivmelendirilir. Bunu takiben e-demeti salındırıcıdan geçer; bu cihaz, hava boşluğu ile birbirinden ayrılan iki paralel mıknatıs dizisinden oluşur. Her dizide mıknatıslar, kutup polariteleri her seferinde değiştirilerek ardışık şekilde sıralanmıştır. Salındırıcı içinde oluşan manyetik alanın devamlı değişken yapısı nedeniyle, elektronlar düz gitmek yerine, sinüzoidal bir yol izleyerek elektronları radyasyon enerjisi yaymaya zorlar. SEL, dalga boyu milimetreden x-ray'e (XSEL) uzanan ayarlanabilir, eş fazlı, monokromatik, yüksek akı ve parlaklık değerinde radyasyon üretir.

XSEL'in önemli parametrelerinden biri, x-ışını radyasyonu üzerinde doğrudan bir etkiye sahip olan salındırıcı periyodudur. Şu anda Dünyadaki en büyük XSEL'lerden olan LCLS / SLAC'da, 3 cm'lik salındırıcı periyodu ve enerjisi ~ 14 GeV olan e-demeti kullanılarak, 1,5 A dalga boyunda çıkış radyasyonu oluşturabilmektedir. Bu tür yüksek enerjili e-demeti sadece büyük hızlandırıcı tesislerinde üretilebilir. Salındırıcı periyodunu 3 cm'den 300 μm'ye (milim altı periyot) düşürmek, gerekli e-demet enerjisini 1,4 GeV'ye

düşürebilmektedir. Sonuç olarak, daha kompakt e-demet kaynakları kullanılabilir ve XSEL'ler özel uygulamalar için kolayca kullanılabilir hale getirebilirler. Başka bir bakış açısıyla bakıldığında, milim altı periyotlu salındırıcı, yüksek enerjili elektron hızlandırıcıları ile birleştiğinde, bilimdeki yeni keşiflere yol açacak gama ışınları gibi daha yüksek enerjili radyasyon üretebilecektir.

Bu çalışmada, milim altı periyotlu salındırıcı tasarlanacak ve prototipi üretilecektir. E-demet buharlaştırma, triyot püskürtme ve foto/e-demet litografi sistemleri kullanılarak nano/mikro boyutlu mıknatıslar sentezlenecektir. Sentezlenen mikro mıknatıslar, bilgisayar modellemeler sonucunda en uygun boyut ve dizlim kombinasyonuna karar verilerek, salındırıcı içine monte edilecektir. Sentezlenen gelişmiş mikro mıknatıslar, yeni nesil manyetik mikro-aletlerin yapı taşları olarak da kullanılabilecek olması unutulmamalıdır. Projenin nihai hedefi, çalışan bir XSEL'de salındırıcının test edilmesidir.

To my family for their patience, support, and love,

and friends for their support and precious advice

ACKNOWLEDGEMENTS

Firstly, I would like to express my gratitude and thanks to my co-advisor and the main instructor of the project, Assoc. Prof. Dr. Ozan Akdoğan. It was a very tough three years that I have experienced a lot during that period. I have been driven to a better researcher under his mentorship, support, guidance, and patience. I'm proud and happy to be able to hold the promise that I gave at the beginning. Thank you for believing in me and supporting me no matter what. Thanks to Burç Mısırlıoğlu, the advisor of the project, for his encouragement, advice, and support he showed to me through my research.

Secondly, thanks and gratitude to all the professors and the instructors in the Material's Science and Nanoengineering Program. Thanks to Gözde İnce for the encouragement at the very beginning of my journey. Thanks to "Mali Hoca" for having such a brilliant personality and wisdom. Thanks to Cleva Ow-Yang for always pushing me to be better in my studies. Thanks to Melih Papila for the motivational talks when I felt exhausted. And thanks to all professors, I might forget, for helping me to achieve my goals.

Thanks to the people, I worked together at the Institut NEEL in Grenoble, France. Thanks to Nora Dempsey, Frederico Orlandini-Keller, Georgiana Irina Groza, Thibaut Devillers, and Richard Haettel for the support, help, and hosting me in your labs. I hope our paths would cross again in the future.

Special thanks to all my friends who supported and helped me multiple times. Thanks to Onur Zırhlı for the accompany and the help during the period. Thank you for being there whenever I needed. Thanks to Omid Moradi for pieces of advice on many different topics that helped me understanding better. Thanks to Ali Tufani for the insane support. Thanks to Berke Tonoz, Tuğçe Akkaş, Cemre Irmak Kayalan, Semih Pehlivan, Rana Altay, Can Egil, Yelda Yorulmaz for the support and friendship you showed me.

Finally, I have to say my special thanks to my family for supporting me and my efforts, the unlimited love, patience, encouragement, advice, and many things during these three years. I could not finish my studies without you.

This project is supported by TÜBİTAK project:118F319 and Campus France (PHC BOSPHORE project 42620TH)

TABLE OF CONTENTS

LIST OF FIGURES

LIST OF TABLES

LIST OF ABBREVIATIONS

FEL – Free Electron Laser

X-FEL – X-Ray Free Electron Laser

SACLA – Spring-8 Angstrom Compact free electron LAser

LCLS – Linac Coherent Light Source

DESY - Deutsches Elektronen-Synchrotron

CLIO – The Centre Laser Infrarouge d'Orsay

μ_s – Spin magnetic moment

H_d – Demagnetizing field

λ_u – Undulator period

T_c – Curie temperature

H – Applied magnetic field

M_s – Saturation magnetization

M_r – Remanent magnetization

NdFeB – Neodymium Iron Boron

FePt – Iron Platinum

SEM – Scanning Electron Microscope

XRD – X-ray Diffraction

EDS – Energy Dispersive Spectroscopy

VSM – Vibrating Sample Magnetometer

SQUID – Superconducting Quantum Interference Device

UV – Ultra Viole

1. INTRODUCTION

The developments in the light of studies done on radiation sources have a significant impact on our lives. In 1917, Albert Einstein studied the focused light beams and claimed that atoms could be in a higher energy state than the ground state by applying some external energy and stated that if a photon collides with an excited electron with the same wavelength, they will have the same frequency and phase (Einstein, 1917). It is the first study for the theory of the invention of lasers named from the initials of "Light Amplification by Stimulated Emission of Radiation." During World War II, scientists grew their interest in radiation energy more. In 1945, the first study started with synchrotron radiation in the Research Laboratory of the General Electric Company (Blewett, 1998). Afterward, Motz studied generating coherent radiation by using an alternating magnetic field, undulator radiation (Motz, 1951). The idea was to use alternating magnetic fields or so-called undulators to force electrons to follow a sinusoidal path to emit electromagnetic radiation. In these studies, incoherent radiation was obtained in the millimeter range and with a peak power of 10 W (Motz, Thon, & Whitehurst, 1953). In the early 1970s, the 4^{th} generation light source, the Free Electron Laser (FEL), was invented later on with the developments of synchrotron and undulator radiation sources by John Madey (Madey, 1971). FELs can produce tunable coherent radiation with a wide range of electromagnetic spectrum from centimeters to X-ray level (X-FEL) with a peak power of 10^{10} W in pulses. It also has a repetition rate of 27 kHz with a wavelength of approximately 0.5 Å and pulse duration, the time it takes light to travel 1 μm, of 0.3 fs (Schneidmiller & Yurkov, 2011). So, FELs shed light on an ultra-small world (below 100 nm) and ultra-fast (down to fs). Thus, scientists grew their interest in its applications more after the invention of the FEL.

Electrons come out from an electron gun (electron source) in the FEL systems. Then, electrons are accelerated almost to the speed of light with the help of a linear accelerator or so-called Linac. These accelerated electrons pass through an insertion device called an undulator which is constructed by permanent magnets having a gap between each with alternating polarity. The magnetic field created by the magnets in the undulators forces the accelerated electron beam to follow a sinusoidal path. With each oscillation, the electron beam emits coherent radiation. Then, electrons are dumped, and

the light is directed to the experimental devices to operate an investigation. The schematic of an FEL system is shown in Figure 1.

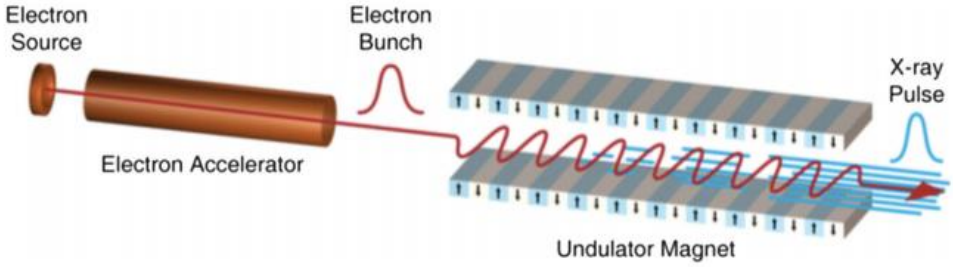

Figure 1 A schematic of an FEL system (Pellegrini, Marinelli, & Reiche, 2016)

At present, there are a couple of facilities in different countries working with the X-FEL systems, such as SACLA (Japan), LCLS (the U.S.A.), DESY (Germany), FERMI (Italy), and ELSA&CLIO (France). The current state of the art of XFEL'S; LCLS/SLAC (Figure 2) uses an undulator period of 3 cm and creates an output radiation wavelength down to 1.5 Å using an electron beam with an energy of approximately 14GeV. However, this kind of high-energy electron beam could only be generated in large accelerator facilities. The properties of the largest three FEL facilities are shown in Table 1.

Figure 2 The bird's eye view of LCLS/SLAC (3.2 km length)

Table 1. The properties of the three largest FEL facilities (Shintake, 2007)

	Euro-XFEL	LCLS (SLAC)	XFEL/Spring-8
Wavelength	6 – 0.085 nm	1.5 – 0.15 nm	6 – 0.08 nm
Beam Energy	10 – 20 GeV	14.3 GeV	2 – 8 GeV
Main Accelerator			
Accelerator Length	2.1 km	1 km	400 m
Undulator Period	26 mm	30 mm	18 mm
Total length	3.4 km	1.6 km	700 m

Since high-energy coherent radiation can be obtained from the FELs, there are applications in medical science, materials science, the manufacturing industry, and the military. There are some unique applications with FELs, such as investigating protein and hydrogen defect dynamics (Budde, Lüpke, Parks Cheney, Tolk, & Feldman, 2000) and a biopsy of brain tumor (Joos, Shen, Shetlar, & Casagrande, 2000), and soft tissue incisions (Edwards et al., 1994).

These applications are limited because the light source used in the experiments could be generated at large facilities. For instance, only the undulator part of the FELs can be up to 3 km, as shown in Figure 1. Thus, the experiments can be implemented only in the FEL facilities. This study aims to design a sub-millimeter period undulator prototype with an undulator period down to 300 μm from 3 cm. Minimizing the undulator period down to micrometers requires less energy to generate the same amount of radiation in larger facilities.

1.1. Theoretical Background

1.1.1. Origin of Magnetism

The movement of an electrically charged particle creates a magnetic field, thus, a magnetic moment. For instance, a current on a wire creates a magnetic field during the flow. On the atomic level, electrons contribute to the magnetic moment in two ways. They either move around an orbital in an atom, creating an orbital magnetic moment, or spin around their axis that produces a spin magnetic moment. The spin magnetic moment is calculated as

$$\mu_s = -g\frac{e\hbar}{4m} \qquad (1.1)$$

where e is the charge of an electron, h is the Planck constant, m is the mass of an electron, and g(-2) is the g-factor. They create a magnetic field by magnetic dipoles. The generated magnetic field can be represented by the magnetic flux lines as in Figure 3.

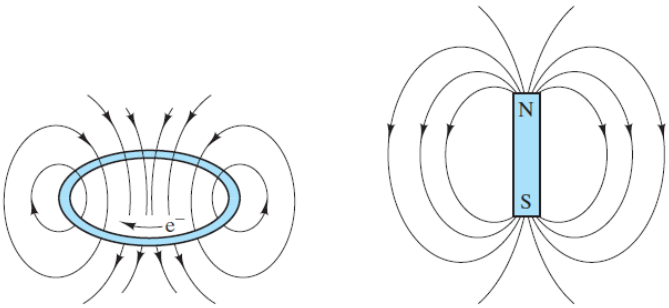

Figure 3 Representation of created magnetic fields by the orbital movement of an electron (left), and the magnetic field distribution of a magnet (right)

All materials have at least one of two types of magnetism mentioned above. The response of electron and atomic magnetic dipoles of the materials can indicate their magnetic behavior by acting differently when an external magnetic field is applied. The magnetic effect originates from the spins of unpaired electrons in orbitals. These unpaired electrons are called magnetization electrons. When there is a paired electron in an orbital, they spin in the opposite direction that cancels out of their spin magnetic moment resulting in no magnetic effect. There are different kinds of magnetic materials such as diamagnets, paramagnets, ferromagnets, anti-ferromagnets, and ferrimagnets. Supposing

each atom in a solid has an independent magnetic moment and is not aligned in the same direction as any of its neighbors. In this case, the solid material will have zero net magnetization. These materials are called paramagnetic materials. Some materials are called diamagnetic when the atoms have no net magnetic moment when no applied field and have a magnetization opposite the applied field. Anti-ferromagnetic materials have adjacent magnetic dipoles aligned in an anti-parallel direction with the same magnitude results in zero net magnetic moments. In ferrimagnetic materials, they have anti-parallel adjacent magnetic dipoles like anti-ferromagnetic materials, but the magnitude is not the same. Thus, ferrimagnetic materials have a net magnetic moment.

1.1.2. Ferromagnetism

In 1925, Pauli claimed that two electrons could not have the same quantum numbers, and it is called Pauli's Exclusion Principle (Pauli, 1925). It also applies to fermions, which are particles with a half-integer spin. Ferromagnetic materials have unpaired electron spins at the atomic level aligned parallel in small regions, called domains, by the long-range ordering phenomenon. In a bulk material, even if a magnetic field is caused by the parallel aligned electrons inside a domain, all domains have randomly oriented. Without magnetizing a ferromagnetic material, the spontaneously magnetized domains cancel out each other, leaving zero net magnetization. The external magnetic field applied causes all the domains with the electrons inside to align themselves in the same direction as the magnetic field in a parallel arrangement, as shown in Figure 4. After the external magnetic field is removed, ferromagnetic materials tend to remain magnetized, called remanence magnetization.

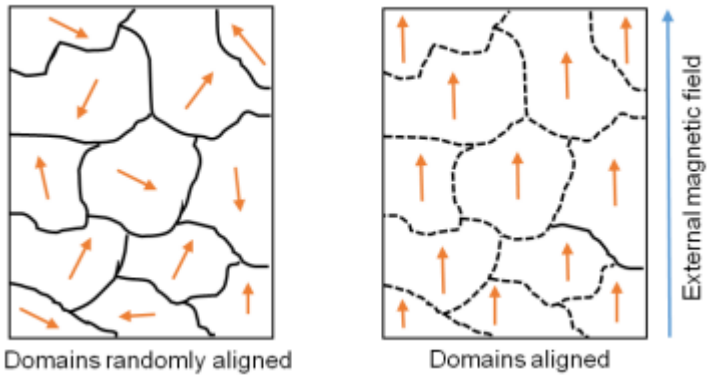

Figure 4 Representation of ferromagnetic domains without (left) and with (right) an applied magnetic field (Nisticò, Cesano, & Garello, 2020)

Temperature is an essential parameter for both the arrangement of spins and for domain magnetization. After a specific temperature, called Curie Temperature (T_c), all ferromagnetic materials behave like paramagnetic. Iron (Fe), nickel (Ni), cobalt (Co) are some examples of ferromagnetic materials with curie temperatures above room temperature.

1.1.3. Magnetic Anisotropy

Magnetic anisotropy is the dependence of magnetic properties in the preferred direction. There are different types of anisotropy; magnetocrystalline, stress, and shape anisotropy.

The magnetocrystalline anisotropy is an intrinsic property and not related to the shape and size of the grains. Magnetization differs when a field is applied along different crystallographic directions, such as the easy axis or hard axis. The total magnetization tends to lie along the easy axis. The reason for forming the magnetocrystalline anisotropy is spin-orbit coupling.

Another type of anisotropy is stress or magnetostriction anisotropy, which depends on the shape of the material. During the magnetization, the demagnetized crystal is affected by a strain while applying a field. Thus, the change in dimension depending on stress during the magnetization is called magnetostriction.

Lastly, shape anisotropy depends on the shape of the material. At the surface of a magnetized material, external magnetic poles are produced. These produce an additional

magnetic field in the opposite direction, called demagnetizing field H_d. Thus, the magnitude is also proportional to the shape of the material.

1.1.4. Hysteresis Loop

A hysteresis loop is an experiment output that demonstrates the magnetic behavior of the measured sample. In other words, it is the scan of the magnetization or change of magnetic moment while changing the external magnetic field. As an output, it derives a moment vs. magnetic field graph including a couple of other parameters, as shown in Figure 5.

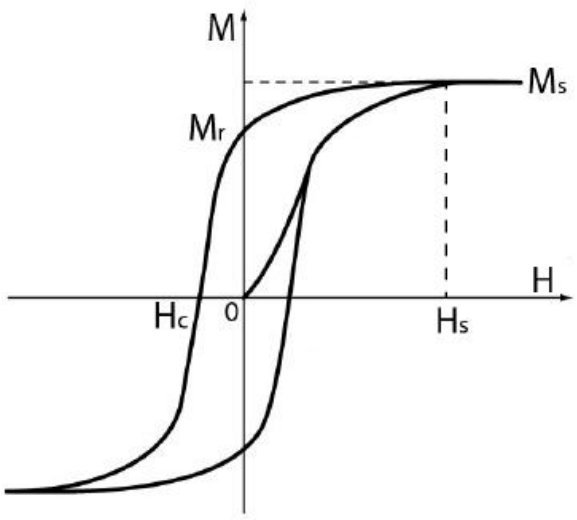

Figure 5 A schematic representation of a hysteresis loop (Arora, 2018)

A non-magnetized ferromagnet would have zero magnetization at the initial point where the applied magnetic field H = 0. After increasing the external field, magnetic flux or magnetization will increase proportionally. At some point, all the magnetic domains of the ferromagnet are aligned along the same direction with the magnetic field, and the magnetization stops increasing even the applied magnetic field continues to increase. This specific point is called saturation magnetization (M_s). When the applied magnetic field is removed, the ferromagnet does not lose all its magnetization. The remaining magnetization is called the remanent magnetization (M_r) or retention point. To obtain zero magnetization again, the external field should be applied in the opposite direction.

The point that magnetization changes its sign represents the coercive field or coercivity (H_c) of the ferromagnet. Lastly, with the alternating applied field, the hysteresis loop is completed.

1.1.5. Iron Platinum (FePt) Alloys

FePt is a hard ferromagnetic alloy on which there are lots of studies had been carried out (Coffey, Parker, & Howard, 1995; Weller et al., 2000; Yu et al., 2000). In recent years, there has been an enormous interest in FePt alloys for the high-density recording media due to their high magnetocrystalline anisotropy. As synthesized FePt alloys have an equiatomic Face Centered Cubic (FCC) crystal structure with a low magnetic anisotropy. Both Fe and Pt atoms have an equal chance to occupy the atomic positions in the crystal. The magnetic properties of FePt alloys are crucial for their applications. The structure transforms from soft ferromagnetic FCC to hard ferromagnetic FCT (Face Centered Tetragonal) phase at high temperatures.

In the FCT structure of FePt alloys, Fe and Pt elements align in consecutive order having an intrinsic property, c/a ratio of 0.963 (a=3.85Å, c=3.71Å). The phase transition from FCC to FCT of FePt alloys requires an annealing procedure. The FCT phase $L1_0$ ordered FePt can provide a magnetic anisotropy almost to the 10^8 erg/cm^3 (Bian, Laughlin, Sato, & Hirotsu, 2000). The high magnetocrystalline anisotropy of the FePt alloys is based on the large spin-orbit coupling in the 5d element and the crystalline ordering of the FCT structure, which is described by ordering parameter, S (Gutfleisch, Lyubina, Müller, & Schultz, 2005; Rong et al., 2006). Also, FePt magnets have natural corrosion resistance, making them even more exciting for many applications.

1.1.6. Undulators

An undulator is a magnetic insertion device that is consisted of two parallel sets of magnets with alternating polarity and a gap in between facing each other, shown in Figure 6. The period of the magnets, called the undulator period (λ_u), is the distance between the centers of two adjacent magnets polarized in the same direction. These alternating magnets create a magnetic field gradient that makes the accelerated electron beam follow a sinusoidal trajectory while passing through the undulator system. Quasi-

monochromatic synchrotron radiation is produced with every oscillation due to the Lorentz Force and Doppler effect. The electron beam emits an electric field while passing through an undulator. Some of the electrons move in the direction of the electric field, while some of them move in the opposite direction. Thus, some of them gain a transverse momentum while others lose. At the same time, oscillating electromagnetic waves that are emitted by the undulator cause the electrons to align with an order. Therefore, the incoherent radiation becomes coherent radiation. This alignment is called microbunching.

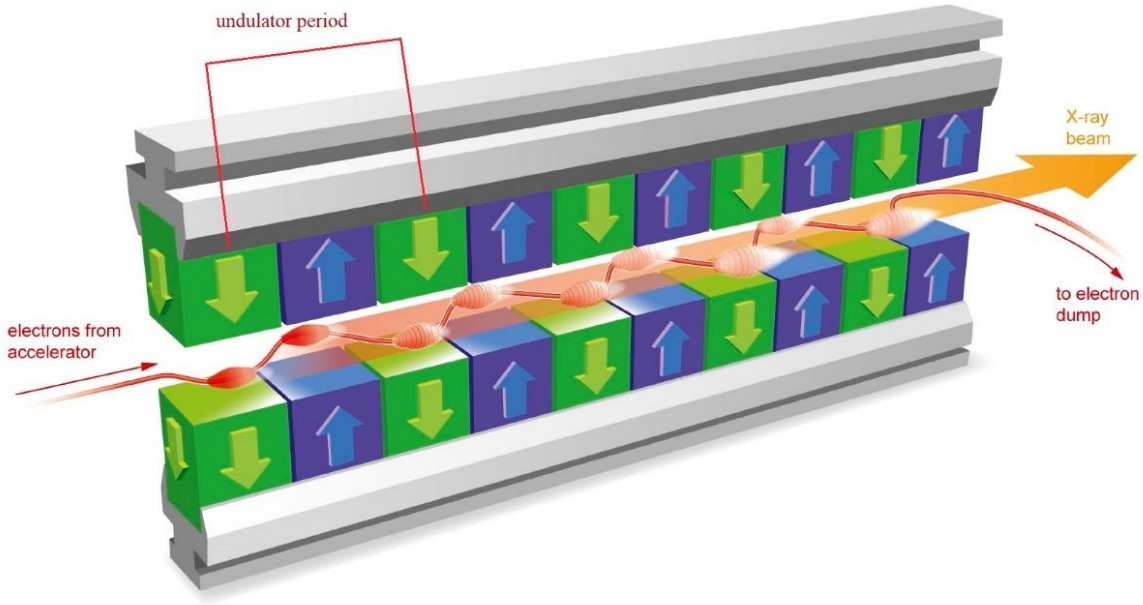

Figure 6 A schematic picture of an undulator

In an undulator structure, the magnetic field is in the form of

$$B(z) = B_y = B_0 \cos(2\pi c/\lambda_u) = B_0 \cos k_u z \quad (1.2)$$

where *B(z)* is the magnetic field in the z-direction, B_0 is the amplitude of the magnetic field, $k_u = 2\pi/\lambda_u$ is the undulator period wave number, and c is the speed of the light. The

undulator magnetic period is an essential factor in tuning the generated monochromatic radiation.

The wavelength of the radiation is calculated by

$$\lambda_{rad} = \frac{\lambda_u}{2\gamma^2}\left(1 + \frac{K^2}{2}\right) \qquad (1.3)$$

where λ_{rad}, λ_u, γ, and K are the wavelength of the radiation, undulator period, Lorentz factor of the electrons, and undulator parameter, respectively.

Also, the undulator parameter, K, is defined

$$K = \frac{eB_0\lambda_u}{2\pi m_0 c} \cong 0{,}93 B_0[T]\lambda_u[cm] \qquad (1.4)$$

where m_0 is the mass of an electron. Thus, the wavelength of the radiation can be tuned by changing the undulator period, λ_u. For current FEL systems, 20 GeV of energy is required to obtain radiation with a wavelength of 1 Å (solid X-ray) with parameters of λ_u = 3 cm and K=2 (Shintake, 2007). For an ultra-small undulator period, K << 1, Eq. (1.4) is reduced to $\lambda_{rad} = \lambda_u/(2\gamma^2)$. Thus, the same radiation can be obtained from only 2 GeV of energy with the undulator period of λ_u = 300 μm, which could be revolutionary since much smaller FELs could be constructed according to the formulations.

2. MATERIALS & EXPERIMENTAL METHODS

2.1. Designing an Undulator Prototype by Micromachining NdFeB Magnets

This method aimed to design an undulator prototype by micromachining commercialized NdFeB magnets. Several different comb-like prototype designs used for micromachining were drawn using AUTOCAD, a computer-aided drawing program, shown in Figure 7.

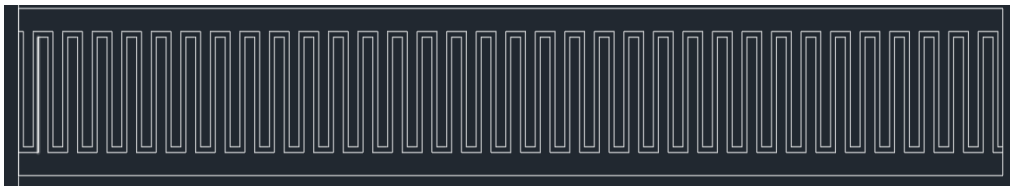

Figure 7 An undulator prototype design, drawn by AUTOCAD.

The period of undulator designs varied from 250 μm to 2 mm. During the experiments, a commercialized 8x10x2 cm, N52 grade, Nickel plated NdFeB magnet was used. The magnet was cut into 1 mm thick slices by wire EDM (Electrical Discharge Machining) machine (Figure 8). Then the slices went through a laser micromachining process in a cleanroom laboratory of Boğaziçi University. Ahmet T. Talaş ran the experiments, technical staff in Boğaziçi University. The laser cutting instrument used for micromachining has an output power of 200 W and works with an unpolarized laser with a wavelength of 1080 nm and a diameter of 16 microns (Figure 9). After the first trials, similar experiments were also tried with femtosecond lasers in UFOLAB in Ankara. Prof. F. Ömer İlday conducted the experiments with femtosecond lasers.

Figure 8 1 mm thick NdFeB slice cut by EDM

Figure 9 The laser cutting instrument in Boğaziçi University

2.2. Synthesizing NdFeB Micromagnets

Nano-thick NdFeB flakes (lateral dimension: ~10 microns) were mixed with a photoresist resin, SU-8, to produce neodymium-iron-boron (NdFeB) micromagnets. At first, NdFeB flakes were synthesized by using the planetary ball milling method. Planetary Ball milling is a mechanical alloying process that allows amorphization and disordering of intermetallics, refinement of grain sizes, and production of well-dispersed oxides (Suryanarayana, 2001). Planetary Ball Milling instruments have a structure that

enables vials to rotate in orbit and around their axes. The direction of the rotation of vials is in the opposite direction to the rotation of vials around their axes, providing a centrifugal force that helps the grinding balls to move inside the vials' wall to grind the powder inside by friction force or crushing between vials' wall and grinding balls. Rotating the vials with the desired energy for a specific time provides desired structure or form of the powder. Another parameter in the process is the ratio of the weight of the balls to the powder. Milling samples with a higher ball to powder ratio will have a shorter time to transform into the desired form. In addition to the ball to powder ratio, dispersant and surfactant usage for milling medium is another parameter for preventing cold welding by adsorbing onto the crushed powder's surface and decreasing the possible agglomeration (Nilay G Akdogan, Hadjipanayis, & Sellmyer, 2010; Salah et al., 2011; Suryanarayana, 2001).

In this research, planetary ball milling was executed by MTI Corporation SFM-1 Planetary Ball Milling Instrument (Figure 10). Stainless steel vials and grinding balls in different sizes were used. Specifications of grinding balls are given in Table 1. In order to synthesize micron sized NdFeB flakes, bulk NdFeB pieces were pounded manually down to small pieces by using a mortar. After grinding, NdFeB bulk pieces were sieved with a sieve of 300 μm holes. Sieved NdFeB powder was put into a steel vial. The ratio of the weight of the balls to powder was set to be 10:1, corresponding to 11 grams of NdFeB powder for 127 grams of stainless-steel grinding balls. Heptane and Oleic Acid were used as dispersants and surfactants, respectively. Stainless steel vials, filled with grinding balls in different sizes, NdFeB powder, surfactant, and dispersant, were fixed into the planetary ball mill instrument. Rotating speed and time were set to be 50 rounds per minute (rpm) and 12 hours, which resulted in NdFeB flakes dispersed in heptane and coated with oleic acid. NdFeB flakes were cleaned from extra oleic acid by centrifugation. Half of a 50 ml tube was filled with NdFeB/Heptane, and the other half was filled with ethanol. The samples were centrifuged at 4500 rpm for 15 minutes. After centrifuging, NdFeB flakes separated from the solution, and the step was repeated three times in total. Afterward, NdFeB flakes were obtained.

Figure 10 MTI Corporation SFM-1 Planetary Ball Milling Instrument

Table 2. Specifications of grinding balls used in the ball milling process.

Diameter of Stainless-Steel Grinding Balls (mm)	Quantity
13,48	2
11,85	4
9,95	6
7,91	19
4,83	34

Synthesized NdFeB flakes were then mixed with an epoxy-based negative photoresist resin, SU-8 forming a 30:70 (%wt.) NdFeB:SU-8 mix. The photolithography technique was used to produce NdFeB micromagnets.

In this method, single-crystal Silicon wafers (100) were used as substrate material. For the sample preparation, 4 ml of NdFeB/SU-8 mix was poured onto a substrate. The substrate was spin-coated firstly at 500 rpm for 7 seconds, then at 2500 rpm for 45 seconds, having an acceleration of 100 rpm/sec^2. After a soft bake on a hot plate at 95°C

for 15 minutes, the sample was exposed to UV light for 12 seconds through a mask, composed of circle designs of 50 μm in diameter. The sample was put in a two-step post-bake session on a hot plate at 65°C for 1 minute and then at 95°C for 5 minutes. Afterward, the sample was developed with a SU-8 developer for 8 minutes. With these parameters, approximately 50μm thick NdFeB micromagnets were obtained. Further details will be discussed in the following chapters.

2.3. Constructing Magnetic Arrays by Commercialized NdFeB Magnets

While producing micromagnets for next-generation ultra-short period undulators, constructing an alternative undulator prototype with commercialized NdFeB magnets was another branch of the primary purpose. In the experiments, Nickel-plated, N45 grade (1.14 T coercivity and 43 kA/m max. energy product), 1 mm, and 3 mm commercialized cube NdFeB magnets were used. The magnets were mounted on a Fe-based steel magnetic plate to be able to facilitate placement. Three different magnetic arrays, up-down array (↑↓↑↓…), Halbach array (↑→↓←↑…), and hybrid array (→↑←↓→…), were thought to be studied by mounting the magnets in a proper order one by one manually. An epoxy-based glue was used to stabilize magnets from magnetic forces. After constructing an array, the magnetic field that was created by these arrays was measured by Scanning Hall Probe (SHP).

Figure 11 Set of 3 mm cubic NdFeB magnets mounted in Up-Down array

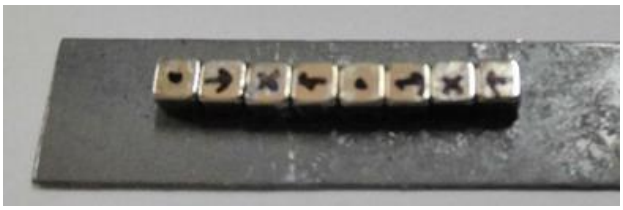

Figure 12 Set of 3 mm cubic NdFeB magnets mounted in Halbach array

After mounting the magnets according to different types of magnetic arrays, a casing was designed by using the SOLIDWORKS program to be able to build an undulator prototype shown in Figure 13. Anycubic Photon LCD-based SLA 3D Printer instrument (see Figure 14) was used to fabricate the cases. It has a sensitivity of 47 μm in the X-Y coordinate. A light-sensitive resin was used as printed material. The minimum resolution of the printing layers in between is down to 25 μm.

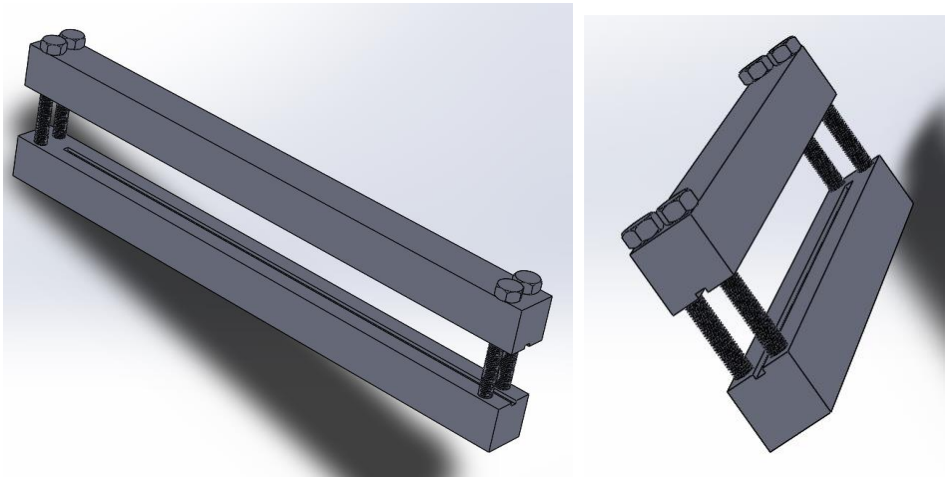

Figure 13 A case model has drawn for placing the magnets

Figure 14 Anycubic Photon LCD-based SLA 3D Printer instrument

2.4. Synthesizing FePt Micromagnets

2.4.1. Synthesizing FePt Micromagnets by E-Beam Evaporation

Firstly, FePt micromagnets were tried to be produced by using the e-beam evaporation technique. E-beam evaporation is similar to thermal evaporation. However, the material is heated up differently. In thermal evaporation, an electrical current is used to heat the boat so that the source material in the boat melts and evaporates. In the e-beam evaporation technique, a stream of electrons or an e beam is aimed at the high purity source material that will be evaporated. This beam of electrons heats the material to its melting point and then evaporates the source material. This electron beam is well confined. One of the advantages of the e-beam evaporation technique is that different source materials can be rotated into the electron beam path so that multiple materials can be deposited sequentially without opening the vacuum system. An e-beam evaporator has two main components. The first is the electron source or electron gun, which produces

the beam of electrons. The second is the crucible, where the source material is contained. There are metal filament, a source of electrons contained within an electron gun, and magnets for focusing the e-beam and directing it towards the crucible. E-beam is generated by heating the metal filament to the point of about 2500 °C. At this temperature, electrons are so energetic that some of them leave from the surface of the filament. These electrons then accelerated towards the source material using a high voltage of electrode, and a set of magnets bend and focus the beam onto the source material to be evaporated. The power level can be controlled by adjusting the filament current. The source material is contained in a small crucible. Depending upon the material being evaporated, the crucible may be made of tungsten, copper, or even ceramic for very high temp deposition. Because the e-beam is well confined in space, only a tiny area of the source material is heated. There can be multiple small rooms for source materials in a copper rotator. In each room, crucibles may contain different source material, which provides multiple layer depositions without breaking a vacuum. The hearth is a rotated holder of copper, which is water-cooled. The water cooling prevents the crucible material from melting and mixing with the source material or the hearth of the holder itself. The experiment schematic is shown in Figure 15.

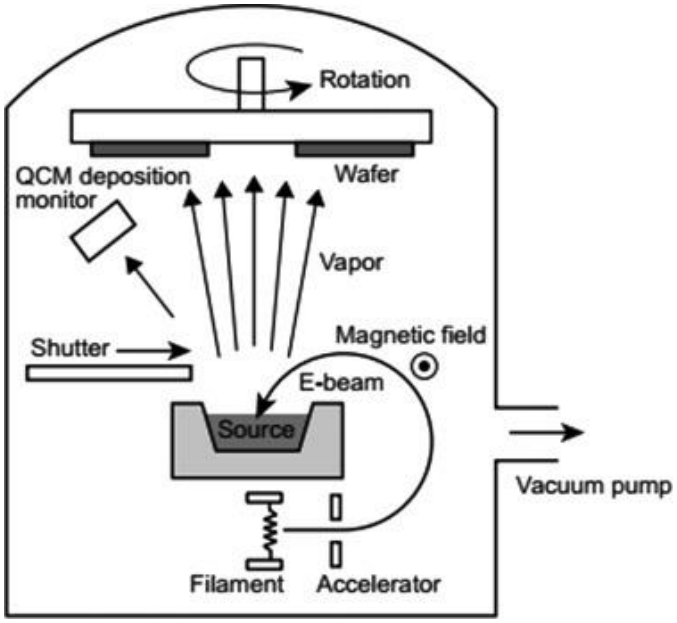

Figure 15 The schematic representation of e-beam evaporation (Oshida, 2013)

In the experiments, the TORR Thermal/E-Beam Evaporator instrument was used. Single-crystal Si wafers (100) were used as substrates. 99.95% pure Iron pellets and 99.99% pure Platinum pellets were used as source deposition materials, where 99.95% pure Chromium pellets were used as a cover layer. A FePt alloy was produced by an arc induction melter. Edmund Bühler GmbH- Compact Arc Melter MAM-1 instrument was used in arc melting. 4,12 gr of Pt and 1,18 gr were melted and mixed to adjust the atomic composition of FePt alloy to 50:50 at %. This alloy was used for deposition. The deposition was executed at room temperature in a vacuum, and at the end, 50 nm of FePt and 15 nm of Cr layers were deposited onto Si substrate.

2.4.2. Synthesizing FePt Micromagnets by Sputtering

After e-beam evaporation trials, synthesizing FePt micromagnets was decided to be continued by the DC magnetron sputtering technique. This technique relies on removing particles from a target material and directing the particles towards a substrate to be deposited as a thin film. The sputtering process is caused by an energetic ion (Ar^+) bombarding created by a plasmatic atmosphere. In addition to particle removal, secondary electrons are also emitted by the ion bombardment, which helps to maintain the plasma in the chamber. The use of magnetrons in sputtering leads to an increase in the chance of atom-electron collision, deposition rates, and a decrease in substrate heating while sputtering. These magnetrons were put under the target material, which was coordinated as one in the center axis of the target and the other in the target material's outer edge. These magnets were put in a reverse pole position, which creates a magnetic field, helping to directly remove particles towards the substrate and help the ions be denser in the target material's surface that allows the ion bombardment steady (Kelly & Arnell, 2000). The schematic of DC magnetron sputtering is shown in Figure 16.

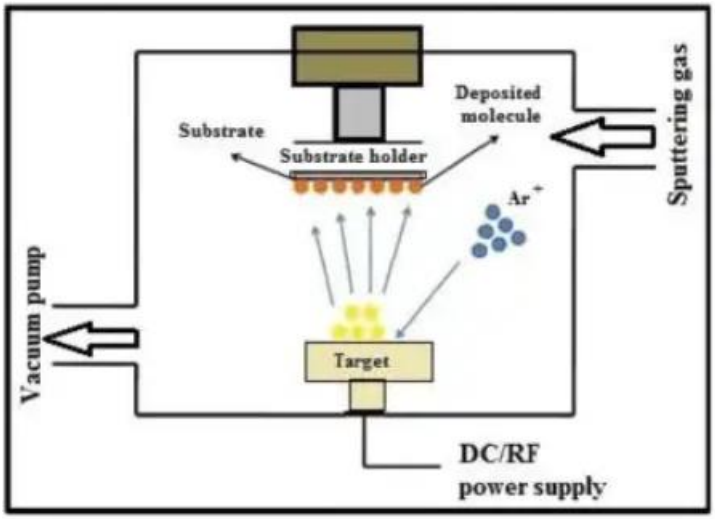

Figure 16 The schematic representation of DC magnetron sputtering

Three different sample sets were synthesized within this work. First (S1), second (S2), and third sets (S3) of FePt thin film samples were synthesized from the hybrid FePt target with two, three, and four pieces of Pt pellets, respectively. This notation will be used in the next chapters. In these experiments, the NANOVAK NVSP-400 Magnetron Sputtering instrument (see Figure 17) was used. Single-crystal Si wafers (100) were used as substrates. Three different hybrid FePt (2" x 1 mm) targets were prepared. Two, three, and four pieces of 99.99% Pt were placed on the racetrack of 99.99% Fe (2" x 1mm) target to achieve Fe: Pt 50:50 %at. composition (see Figure 18). Structures were deposited at room temperature. The vacuum chamber was under base pressure of 5 x 10^{-6} mbar. Sputtering was done under 20 mTorr of Ar gas. Cr (99.99%) buffer and cover layers with thicknesses 5 nm and 15 nm, respectively, were deposited (49-Watt, 0.6 Å/s) onto Si substrate. FePt with 100 nm thickness was deposited (53-Watt, 1.7 Å/s) in between the Cr layers. After the deposition, samples were annealed under Ar/H2 (%5) gas at 650°C for 2, 4, and 6 hours.

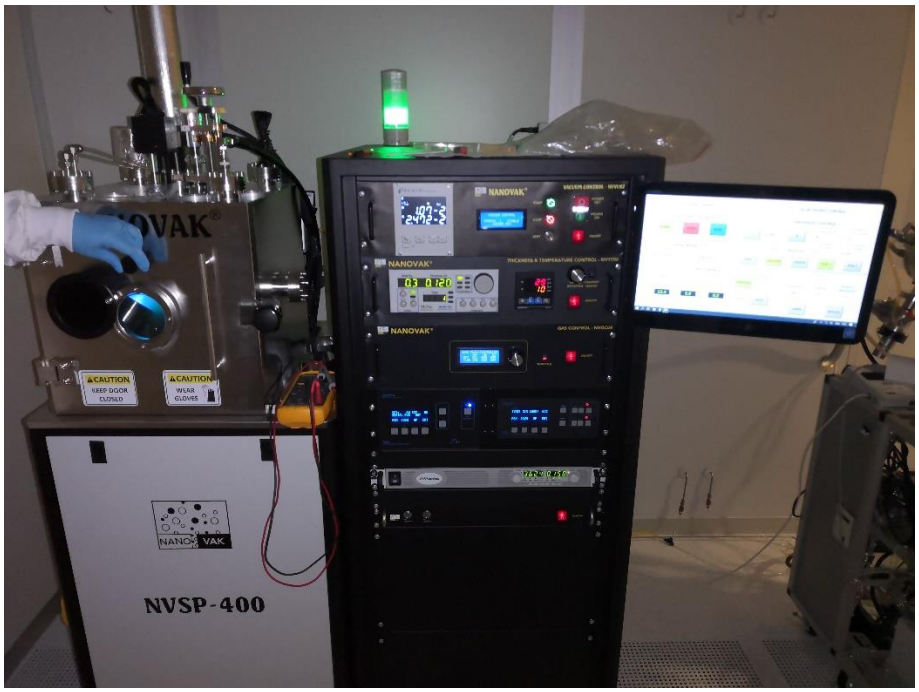

Figure 17 NANOVAK NVSP-400 Magnetron Sputtering instrument

Figure 18 Hybrid FePt targets with 2 Pt pieces (left); 3-Pt pieces (middle); 4-Pt pieces (right)

2.5. Designing An Undulator Prototype With Sputtered FePt Micromagnets by Photolithography

In order to build an undulator prototype, the photolithography technique was used. Photolithography is the process that transfers shapes from a photomask to a surface of a substrate material using UV light. This type of patterning is very advantageous when we

make devices (such as MEMS), interconnections, and structures. A key component in photolithography is the photomask having the desired pattern to transfer onto the substrate. The UV light passes through the photomask with a design. In order to transfer the pattern from the mask onto the substrate, a light-sensitive thin polymer film called a photoresist is used. When the photoresist is exposed to the UV light through the mask, it is patterned (see Figure 19).

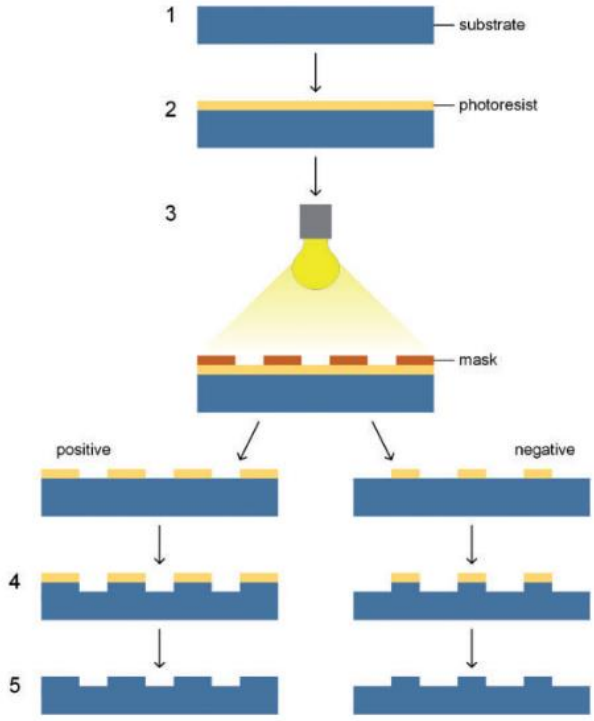

Figure 19 The schematic diagram of photolithography processes (Qiu, Chen, Wang, & Lee, 2014)

In this study, following the sputtering experiments, it was aimed to design an undulator prototype with sputtered FePt micromagnets. Therefore, after successfully synthesizing hard magnetic FePt micromagnets, an undulator prototype would be ready to be developed. Therefore, a photomask (5" x 5" in size, see Figure 20) containing an undulator design with an undulator period varying from 250 µm to 8 mm (see Figure 21) was produced at the Institute of Nano-Technology at Gebze Technical University by using laser lithography (Heidelberg DWL 66 fs laser lithography instrument).

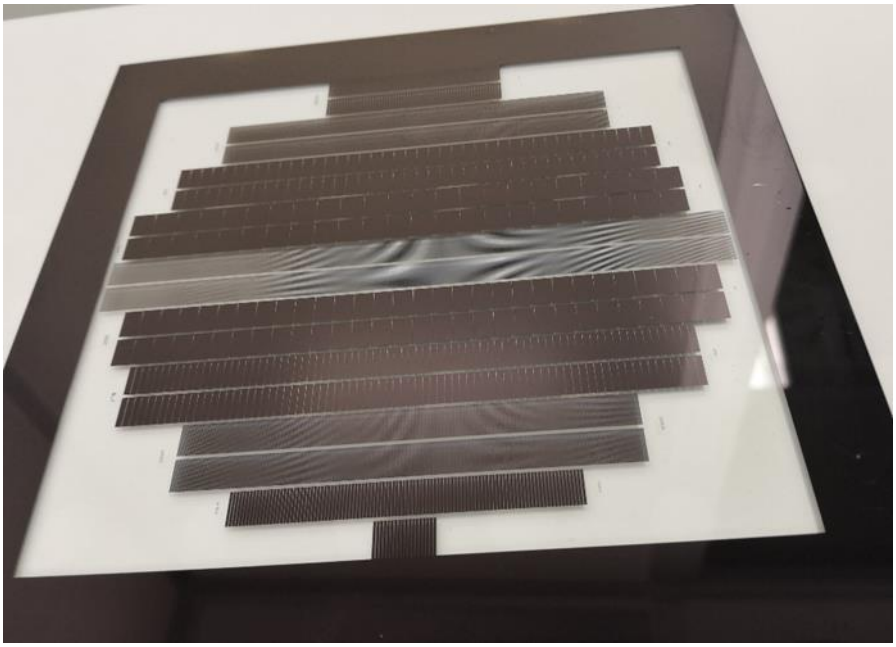

Figure 20 A photomask containing an undulator pattern

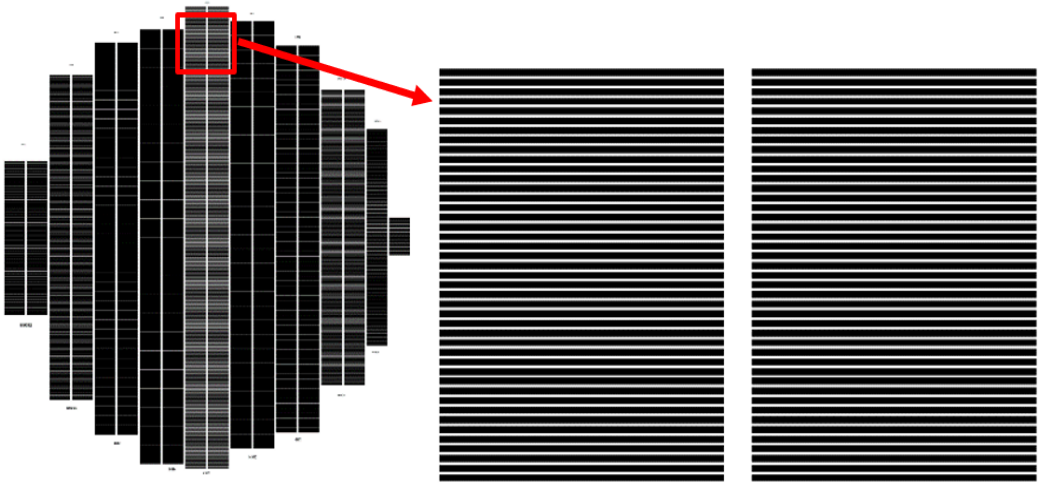

Figure 21 The undulator pattern on the photomask (left); a section from the pattern having 250 µm of the undulator period

The pattern was drawn by using CleWin software. The length of each structure was set to 5 mm. The width of the structures varies from 100 µm to 4 mm. There is a 50 µm gap between each structure and a 500 µm gap between each column.

In the experiment, AZ-nLOF 2070 was used as a negative photoresist. 4" Si (100) wafer was used as a substrate. For the sample preparation, 5 mL of the resist was poured

onto the substrate. The substrate was spin-coated with the resist at 4500 rpm for 45 seconds. After a soft bake on a hot plate at 110°C for 90 seconds, the sample was exposed to UV light for 8 seconds through a mask including undulator designs with undulator periods ranging from 250 μm to 10 mm. The sample was put on a hot plate at 110°C for 90 seconds for the post-bake step and developed with AZ MIF 726 developer for 60 seconds. After that, FePt was deposited onto the prepared resist coated Si substrate by the sputtering method. The remaining resist was removed by a lift-off process using acetone. After the production, samples were annealed at 650°C under Ar/H2 atmosphere for 2, 4, and 6 h, respectively. Lithography experiments were done by Midas / MDA-60MS Mask Aligner. Light microscopy images were taken by Carl Zeiss Optical Microscope.

2.6. Characterization

2.6.1. X-Ray Diffraction (XRD)

X-ray diffraction (XRD) is a technique to identify the atomic, molecular and crystallographic structure and is extensively used in the characterization of materials. The most common uses of XRD instruments include analyzing the crystal structure, quantitative phase composition, finding crystallite size, microstrain, and the residual strain, identifying defects in samples, texture orientation, unit cell parameters, and identify the amorphous materials. All this information is provided by the interaction between X-rays and the sample. The scattering angle and intensity of scattered X-rays are observed by detectors and result in a pattern consisted of scattered intensity peaks as a function of scattering angle. All the information can be collected through the pattern.

In 1912, W.H. Bragg discovered the relationship between the wavelength of an X-ray, the angle of diffraction, and the distance between the internal planes of a crystal shown in Figure 22 (W. H. Bragg, 1913).

$$n\,\lambda = 2d\sin\theta \qquad (2.1)$$

λ is the wavelength of the X-rays, d is the distance between two inner planes, θ is the scattering angle, and n is an integer that indicates the order of diffraction peaks. Bragg's law is used in defining a material using X-rays which are very short wavelengths on the scale of an angstrom. These are aimed at the sample. When the X-rays hit the atoms of the sample, the path of the X-rays is altered. Diffracted X-rays interact with each other and can either have constructive or destructive interference. Destructive interference occurs when the waves are out of phase, meaning that the peak of one wave coincides with the peak of an opposite amplitude in the other way. Essentially the two waves cancel each other out. On the other hand, constructive interference occurs when the waves are in phase, meaning that the positive peaks of the waves are aligned, and the waves are amplified. X-rays being constructive or destructive are determined by the properties of the sample and the angle at which the detector detects the X-rays.

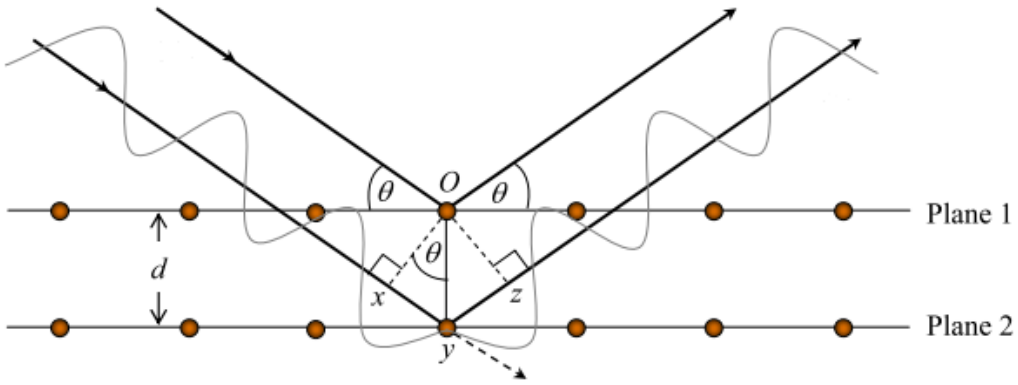

Figure 22 Illustration of Bragg's Law (Thomas, Millican, Okudzeto, & Chan, 2006)

In XRD instruments, the X-ray source or tube is fixed while the detector and the sample are rotated with respect to the source with an angle θ. X-rays produced by the source pass through primary optics that prioritize the X-rays to hit the sample. After X-rays hit the sample, the diffracted X-rays pass through secondary optics and are received to be delivered to the detector. Lastly, in computer, scattered intensity peaks as a function of scattering angle are shown as an output.

In the experiments, Bruker D2 Phaser XRD instrument is used (Figure 23).

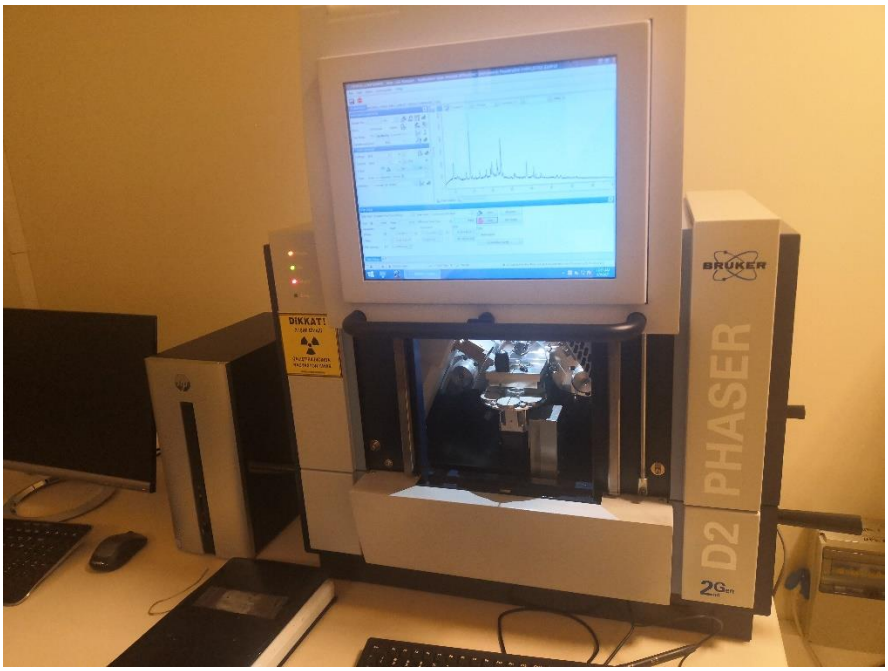

Figure 23 Bruker D2 Phaser XRD instrument

2.6.2. Scanning Electron Microscope (SEM)

The scanning electron microscope (SEM) is a crucial instrument in science that produces magnified images with a variety of microscopic-scale information on the size, shape, composition, crystallography, and other physical and chemical properties of a sample or specimen. The working principle of the SEM instrument in this thesis (Leo SUPRA 35VP FEG-SEM, see Figure 24) starts by generating a focused beam of electrons via emission from an electron source. Usually, the range of energy of the electrons in the beam (E0) is selected to be from E0 = 0.1 to 30 keV (Goldstein et al., 2018). After the beam is created and accelerated to high energy, it is modified through apertures, lenses, and electromagnetic coils. Those parts have the role of making the beam finer by reducing its diameter and scanning in an x-y pattern to place the beam at close, precise locations on the specimen. There are different outcomes from the interaction between the electron beam and specimen at these locations, which are backscattered electrons (BSE) and secondary electrons (SE), Auger electron, and X-rays.

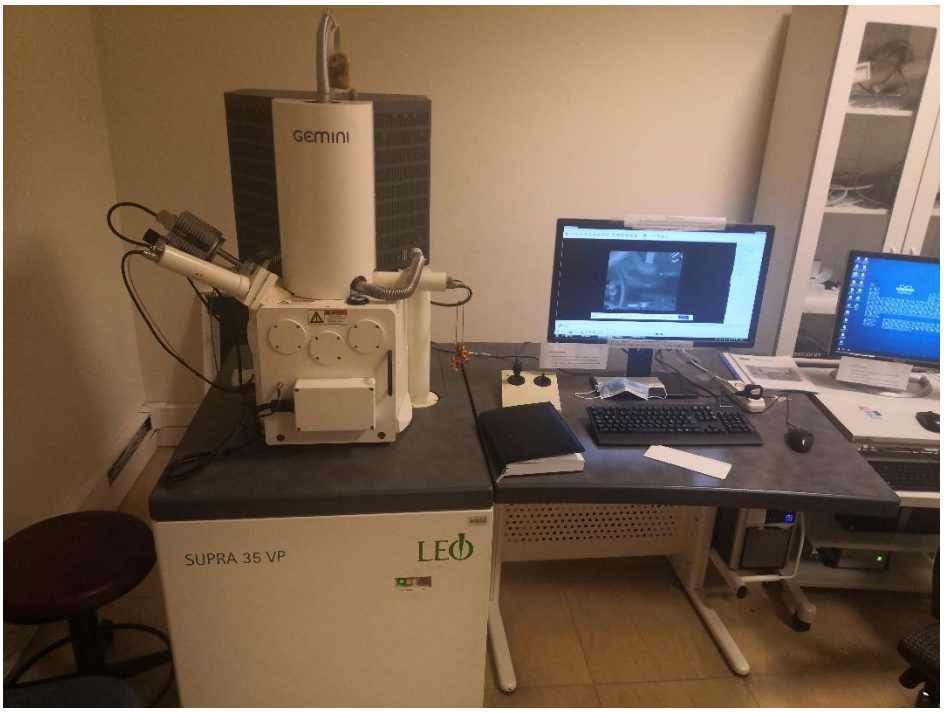

Figure 24 Leo SUPRA 35VP FEG-SEM instrument

When a beam electron interacts with the electric field of a specimen atom electron, inelastic interaction occurs. As a result, an energy transfer and a potential expulsion of an electron from that atom arise as a secondary electron (SE). Since the energy loss, secondary electrons have an energy of less than 50 eV. After an expulsion, an X-ray characteristic of the energy transfer can be obtained when a higher-level orbital fills the vacancy from that secondary electron. When a beam electron interacts with the electric field of the nucleus of a specimen atom, elastic interaction occurs. As a result, the electron beam changes its direction with retaining the same energy. If the direction is back out of the sample, it is called backscattered electron (BSE). SEs and BSEs are coming from different parts of the sample. Thus, the information from the SEs and BSEs also differs. BSEs carry the information from a deeper region of the sample. In BSE images, a higher atomic number results in a brighter sample in the image. In addition, it is possible to obtain essential information on crystallography or topography from the BSE images. SEs, however, arise from surface regions. Thus, SE imaging carries more information about the surface of the sample. With the sum of both elastic and inelastic interactions, the electron beam has effects on the interaction volume shown in Figure 25.

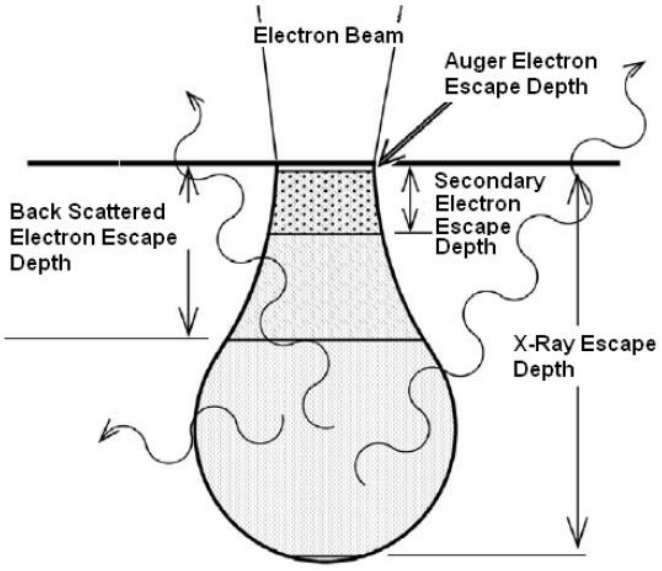

Figure 25 The illustration of an interaction volume

After the interactions, released electrons are collected by different detectors in the chamber. A positively charged detector attracts the SEs and collects them from all directions, while the BSE detector only collects the inelastically scattered electrons from the condenser lens.

2.6.2.1. Energy Dispersive Spectrometer (EDS)

Energy Dispersive Spectrometer is a commonly used technique to obtain qualitative or quantitative information on the chemical composition of the specimen by X-ray lines. It is a valid measurement for elements with atomic number greater than 3. As mentioned above, while the ionization of the atoms of the sample by bombarded with an e-beam, one of the interaction outputs is the X-ray emissions. When bombarding the atoms with a high-energy e-beam, detached electrons of the atom create a vacancy filled by one of the outer shell electrons. Thus, the atom will lower its energy, and the energy difference will be observed as radiation at different wavelengths. The energies of the X-ray radiation are collected by the EDS detector that counts X-rays with every wavelength. The qualitative measurements are done by measuring every characteristic radiation at unique wavelengths that give information on which elements are present or not. On the

other hand, measuring the intensities of these counted X-rays will give quantitative information on the amount of the elements in the sample or the composition of the sample.

The EDS system used in the experiments was installed into the SEM instrument that was used for the characterization.

2.6.3. Vibrating Sample Magnetometer (VSM)

Vibrating Sample Magnetometer (VSM) is the device that measures the magnetic behavior of the materials and operates based on Faraday's law of induction which explains that there will be an electric field produced by changing the magnetic field. The working principle of the VSM starts with sample preparation. The sample is placed in a constant magnetic field. Then, the domains or individual spins of the sample will be aligned and magnetized under the constant magnetic field if it is a magnetic material. After that, a magnetic field, so-called the stray magnetic field, is produced by the magnetic dipole moment of the sample. As the sample is vibrating in the direction of up and down, a set of pick-up coils around the sample detect the change in the stray magnetic field as a function of time. The induction current produced by Faraday's law of induction is amplified by a transimpedance amplifier and lock-in amplifier. A software program helps to convert the changes in signals to a moment versus field (M-H) curve, in other words, hysteresis curve. Quantum Design PPMS 9T VSM instrument was used in the experiments.

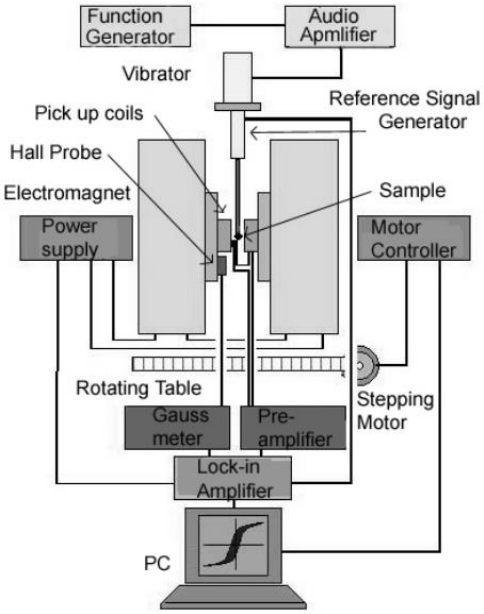

Figure 26 Working principle of VSM (Baruwati, 2015)

2.6.4. Superconducting Quantum Interference Device (SQUID-VSM)

The basic working principle of SQUID is the same as VSM. In SQUID, instead of pick-up coils, there is a superconducting pick-up coil circuit. Also, the magnetic flux is detected by a superconducting quantum interference device. However, it is also based on principles called Josephson Effect or Josephson Junction (JJ) and the magnetic flux quantization. JJ is created by separating two superconductors with an insulating barrier or gap where electron pair waves called Cooper pairs that also carry a superconducting current are tunnelling through. Without any voltage running through the device, the current is proportional to the phase difference between the wave functions represented Cooper pair.

Two Josephson junctions connected parallel on a ring between two superconduction wires (see Figure 27). The junctions have a characteristic critical current which is the maximum current that can be able to flow through them. By applying a current to the device, half the current flows one way while the other half flows the other way. Therefore, the maximum current that the device can take is twice the critical current. On the other hand, by applying a magnetic flux through the device, a phase difference between the opposite sides of the ring is established since the superconducting current

and the induction current that is created by the applied flux will cancel each other in one junction, be added to each other in the other junction. As a result, a voltage between the two ends of the ring is produced.

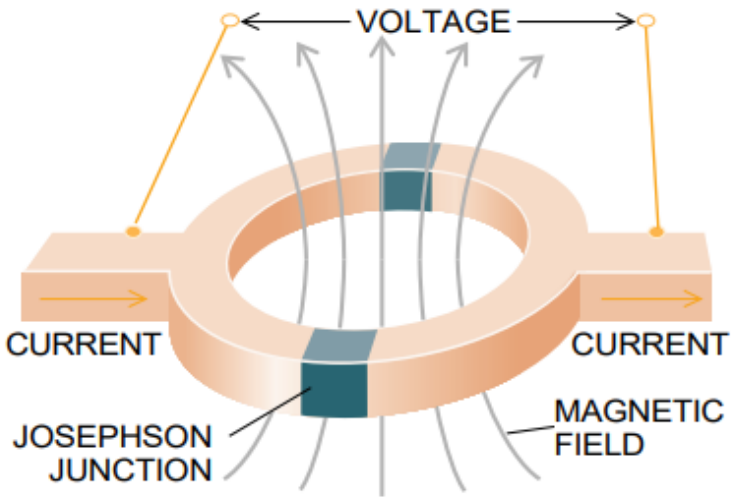

Figure 27 A superconducting ring formed by the two Josephson junctions (Vinet & Zhedanov, 2011)

At this point, quantization magnetic flux takes place. The circulating current will increase the proportions of magnetic flux until half the quanta. Since the circulating current is proportional to energy, it is favourable to reverse the direction of the flux but retaining the magnitude. Then it restores its energy, and after one integer quanta, the flux is returned to zero. The change in the magnetic field leads to the critical current oscillates between a maximum and a minimum value. The maximum value is the integer flux quanta, while the minimum is half the flux quanta. This quantum interference effect provides us with a digital magnetometer, so-called the SQUID magnetometer. In the experiments, Quantum Design MPMS 3 instrument was used (see Figure 28).

Figure 28 Quantum Design MPMS 3, VSM-SQUID instrument

3. RESULTS AND DISCUSSION

3.1. Undulator Prototype by Micromachining NdFeB Magnets

A commercialized N52 grade NdFeB magnet was cut into 1 mm thick slices by a wire EDM. Afterward, the 1 mm thick NdFeB slice went under a micromachining process by laser cutting instrument. The aim was to cut the slice in the design of a 5 mm long undulator, as can be seen in Figure 7. When the micromachining process was over, the sample was observed with a light microscope (see Figure 29).

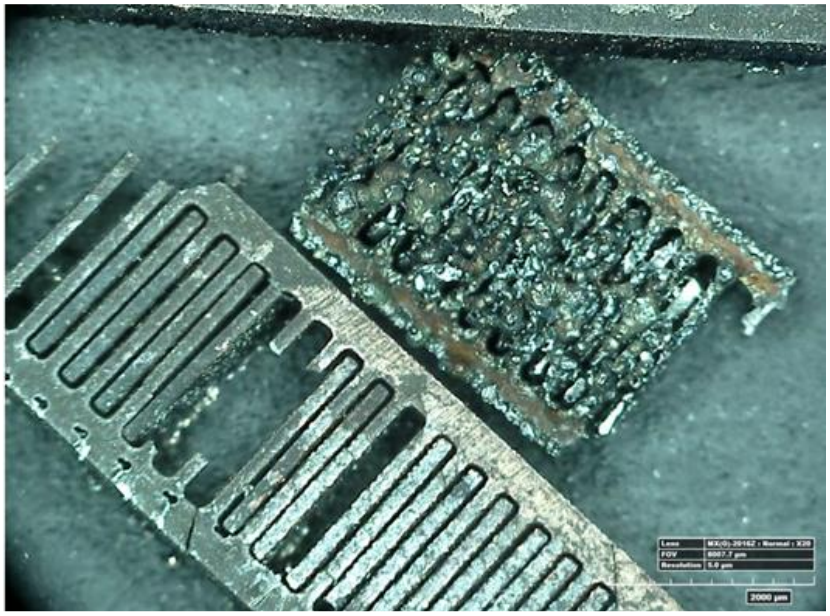

Figure 29 Image of micromachined NdFeB with an undulator design

It can be seen from Figure 29 that the laser cut through the front surface of the NdFeB magnet without any deformation. On the other hand, the surface that the laser exited was deformed. It can be stated that the deformation occurred because of the refractive index difference between the NdFeB and the air resulting in scattering of the laser that creates the deformation on the back surface of the NdFeB. In order to prevent it, two separate 1 mm thick NdFeB slices were stuck together, and the refractive index was thought to be the same between these slices. The same procedure was applied and seen that the two NdFeB slices were conglutinated together because of the high-energy

laser. In addition, multiple microcracks were observed after a micromachining procedure since 1 mm thick NdFeB slices were too fragile and stress-sensitive (see Figure 30).

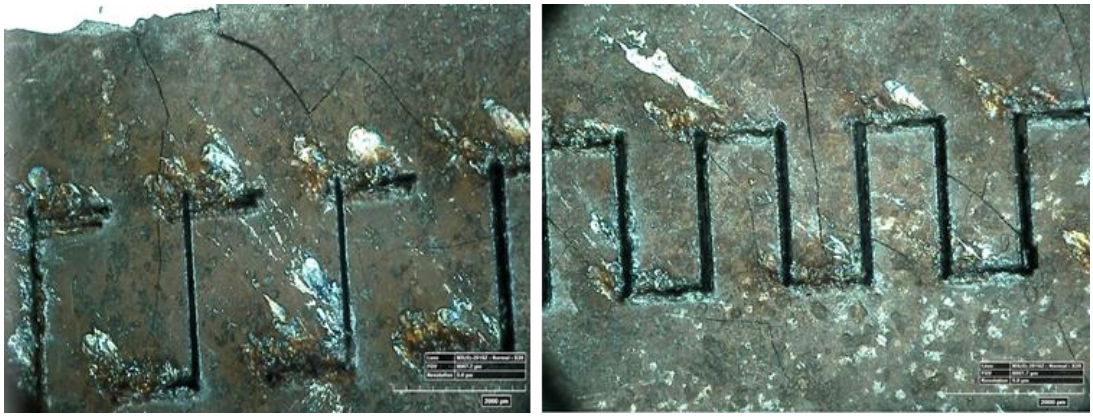

Figure 30 Multiple microcracks on the surface of the 1 mm thick NdFeB surface

After a couple of trials, the procedure continued with the femtosecond lasers in UFOLAB, Ankara. In experiments, it was observed that it could be possible to process the slices without any deformation, shown in Figure 31. However, the parameters for the experiment were variable while the laser was passing through the layers. The laser proceeds in the slice as an hourglass shape as a result of diffraction. The laser broadens above and below the focus point. The speed of broadening is inversely proportional to the focus distance. The smaller the focus distance results in faster the broadening. The focus distance of the femtosecond lasers used in the experiments was 23 µm. Therefore, the thickness of the slices was too thick that prevented the laser from processing deeper. The experiments stopped since no thinner NdFeB slices were produced.

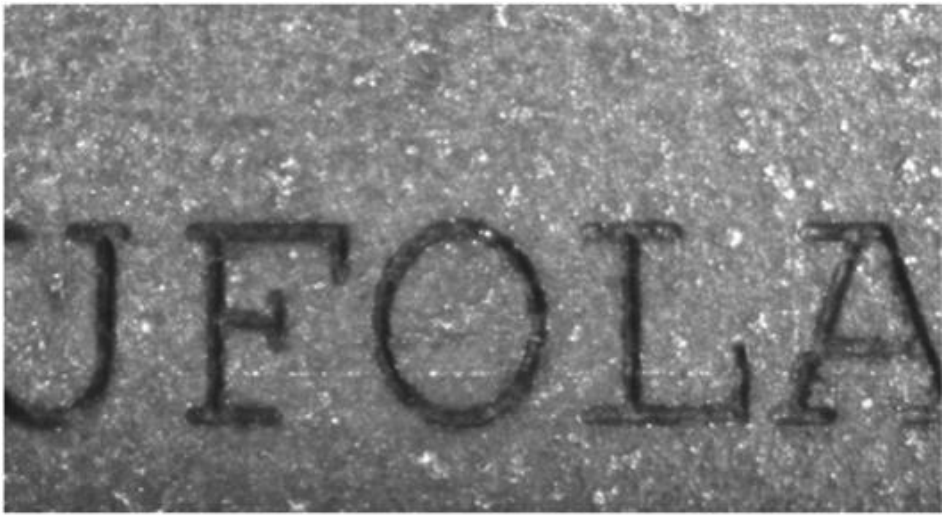

Figure 31 The surface of the NdFeB sample processed with femtosecond lasers

3.2. NdFeB Micromagnets

Nano-thick NdFeB flakes were obtained after ball milling. Nano-thick NdFeB flakes were mixed with a photoresist resin, SU-8, to produce neodymium-iron-boron (NdFeB) micromagnets. After a photolithography procedure was applied, 50 μm thick cylinder-shaped NdFeB/SU-8 micromagnets with a diameter of 50 μm were obtained. Produced micromagnets were examined under the scanning electron microscope and light microscope (see Figure 32 and Figure 33).

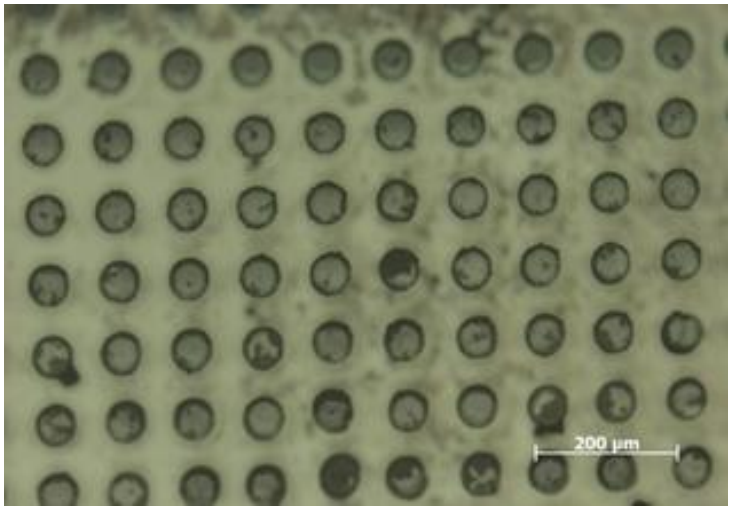

Figure 32 Light microscope image of nano-thick NdFeB/SU8 micromagnets

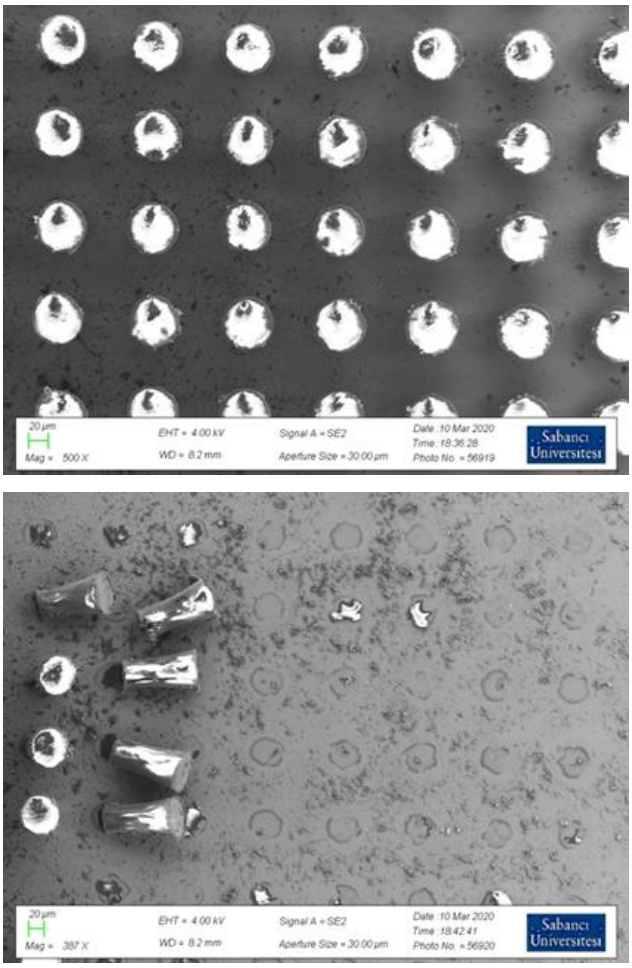

Figure 33 SEM images of nano-thick NdFeB/SU8 micromagnets

It can be stated that the cylindrical NdFeB/SU-8 micromagnets onto a Si substrate were successfully produced. However, as seen from the SEM images, some of the NdFeB/SU-8 micromagnets were detached from the substrate's surface. Nilay G. Akdoğan et al. conducted the same study in 2011. The XRD pattern and the SEM image of NdFeB flakes from the study are shown in Figure 34 and Figure 35. VSM measurement of that study is also shown in Figure 36. Although there were difficulties to be attached to the substrate, the NdFeB/SU-8 mix microstructures were fabricated successfully.

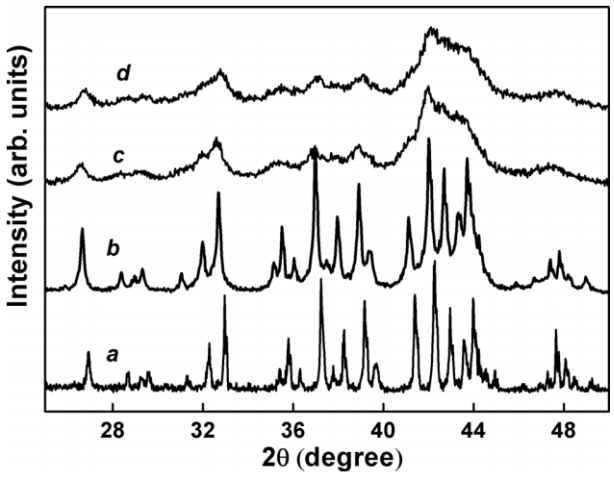

Figure 34 The XRD data for homogenized $Nd_2Fe_{14}B$ alloy (a), milled in heptane (b), additional six hours with oleic acid (c), and 12 hours milling with oleic acid (d) (Nilay G. Akdogan, Li, & Hadjipanayis, 2011)

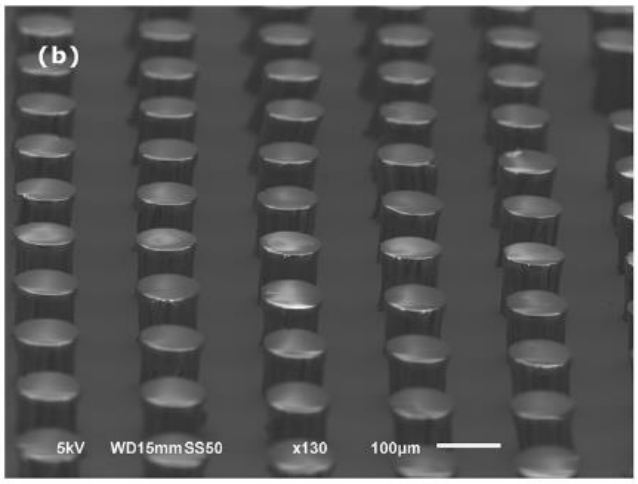

Figure 35 SEM image of nano-thick NdFeB flakes loaded to SU-8 (N. G. Akdogan & Akdogan, 2019)

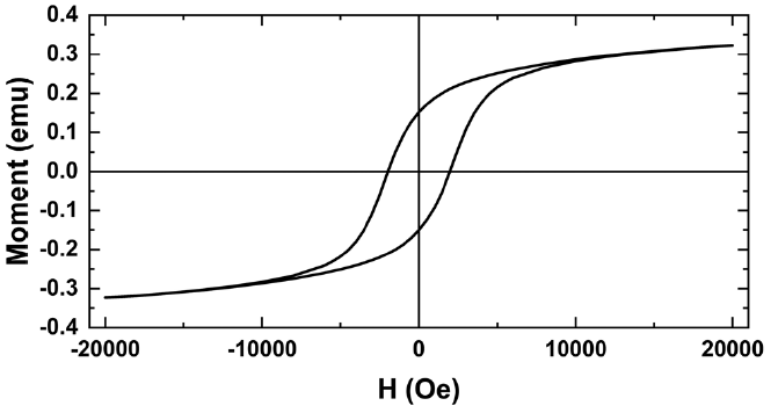

Figure 36 Hysteresis loop of NdFeB/SU-8 Mix (N. G. Akdogan & Akdogan, 2019)

3.3. Magnetic Arrays With Commercialized NdFeB magnets

In this part, commercialized N45 grade Nickel-plated 3 mm cubic NdFeB magnets were mounted manually according to two different magnetic arrays, Up-Down and Halbach Arrays. NdFeB magnets used in the experiments had a coercivity of 1.16 T and a magnetic moment of 43 kA/m. During the mounting, a Fe-based plate was used as a magnetic surface to mount the magnets easily. After the mounting process of the up-down array, the magnetic field map of the structure was measured by a homemade Scanning Hall Probe (SHP) shown in Figure 37. From the results, it can be stated that the magnetic field followed a sinusoidal path during the scanning in the y-plane. Akdogan et al. carried out a study examining the magnetic field mapping simulations of sub-millimeter undulators with different magnetic arrays by the simulations using the RADIA program shown in Figure 39 and Figure 40. (N. G. Akdogan, Polat, & Akdogan, 2020). During the simulations, the magnet thicknesses vary from 10 µm to 100 µm, and the gap between the magnet arrays varies from 10 µm to 400 µm. The experimental results of the magnetic field map of the Up-Down array measured by the SHP matched the results of simulations (see Figure 38).

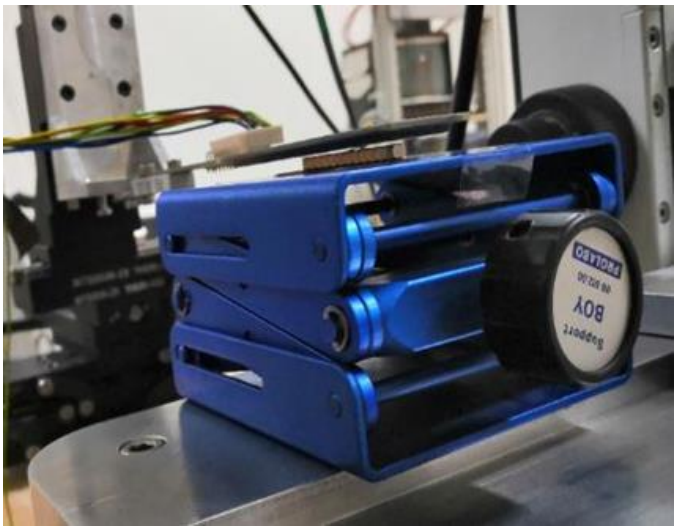

Figure 37 Scanning Hall Probe experimental setup

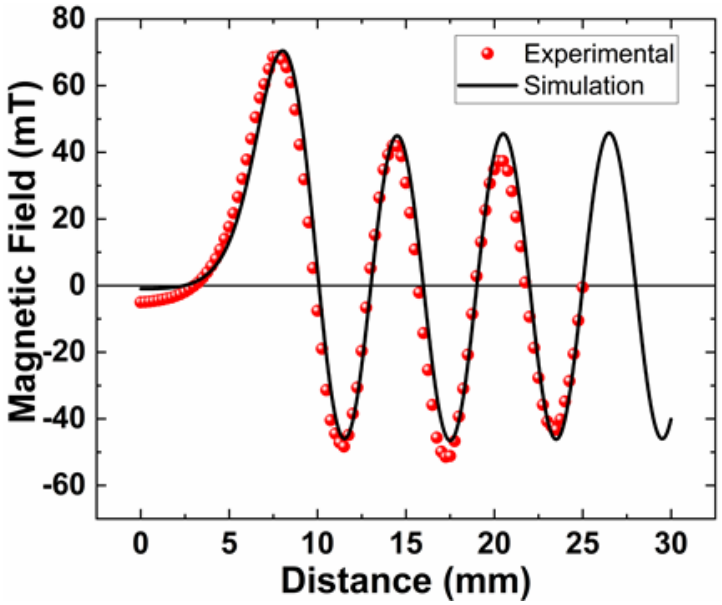

Figure 38 The magnetic field mapping of Up-Down magnetic array mounted with 3 mm cubic NdFeB magnets

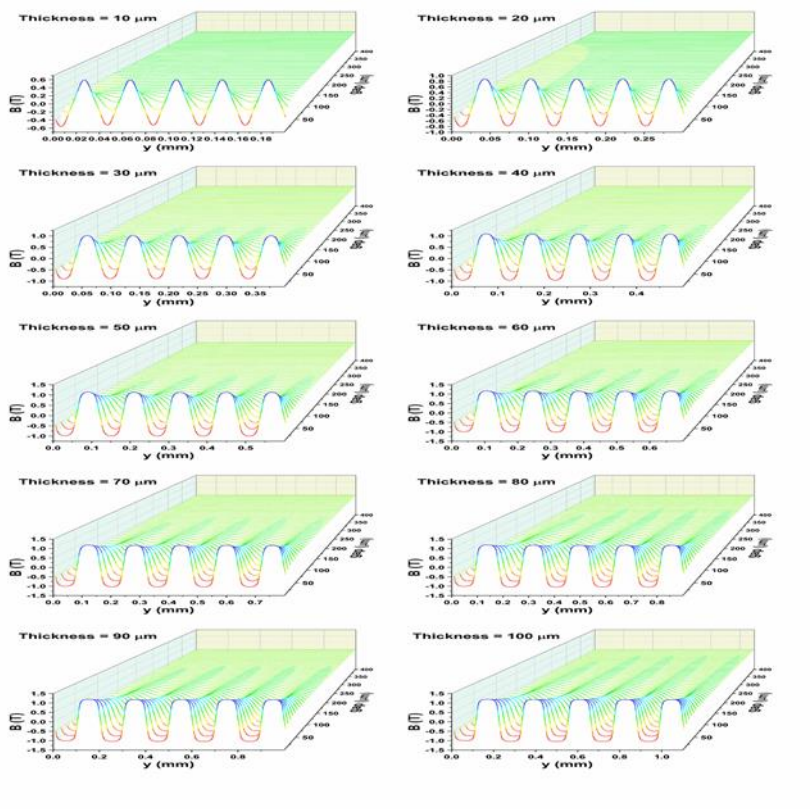

Figure 39 Simulation of Sub-millimeter undulator with Up-Down array run by RADIA (N. G. Akdogan et al., 2020)

From the simulations for the Up-Down magnetic array, it is observed that the magnetic field wave path started to follow a triangle waveform and then transformed into a non-sinusoidal square waveform when the gap between the magnetic arrays was increasing (N. G. Akdogan et al., 2020).

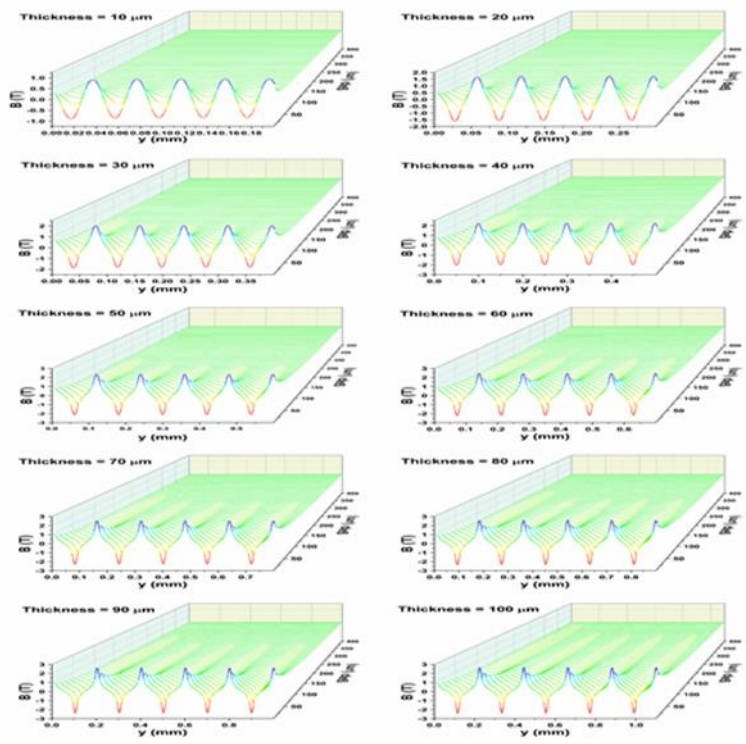

Figure 40 Simulation of Sub-millimeter undulator with Halbach array run by RADIA (N. G. Akdogan et al., 2020)

From the simulations for the Halbach magnetic array, it is observed that the magnetic field wave path started to follow a sinusoidal waveform with the parameters of 10 μm magnet thickness and 10 μm gap between the magnetic arrays (N. G. Akdogan et al., 2020). The thickness of the magnets was also 40 μm. The magnitude of the magnetic field with these parameters was observed to be approximately 1 Tesla. By increasing the thickness of the magnets while retaining the gap, the sinusoidal waveform had defects due to the superposition of two waves.

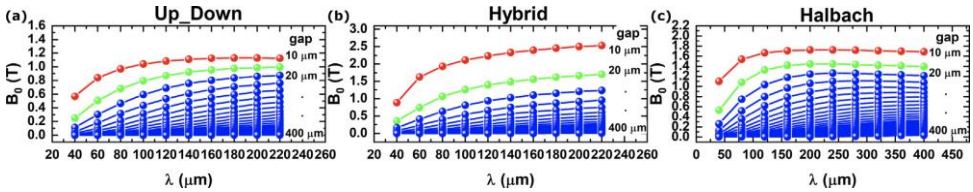

Figure 41 Magnetic Field vs. Undulator Period Graph for three different magnetic arrays (a) Up-Down, (b) Hybrid, and (c) Halbach (N. G. Akdogan et al., 2020)

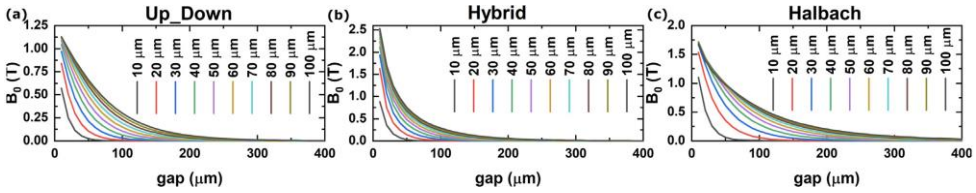

Figure 42 Magnetic Field vs. The Gap Between the Magnets Graph for three different magnetic arrays (a) Up-Down, (b) Hybrid, and (c) Halbach (N. G. Akdogan et al., 2020)

As shown in Figure 41 and Figure 42, an increase in the undulator period led to an increase in the magnetic field, although the magnetic field decreased when the gap between the magnets increased. In addition, the fastest decrease was observed in the Hybrid array, while the slightest decrease was observed in the Halbach array (see Figure 42).

3.4. FePt Micromagnets Synthesized by E-Beam Evaporation Technique

In the first experiments, Fe and Pt elements were put together in the crucible with weights of 4,12 gr Pt and 1,18 gr Fe to obtain 50:50 Fe:Pt (at.)% composition. During the deposition, sparkle formation was observed due to oxidation on the surface of the Fe and Pt source materials. 50 nm of FePt thin film was deposited onto Si (100) wafer. 15 nm of Cr was deposited to prevent oxidation on the surface of the FePt thin film. Produced FePt thin film was examined under XRD (see Figure 43).

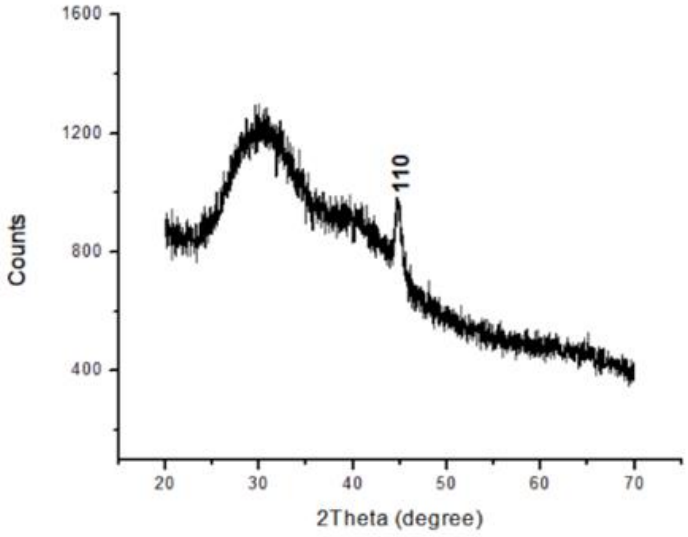

Figure 43 The XRD pattern of deposited FePt thin film (50nm) by e-beam evaporation technique

In the XRD pattern of the produced FePt thin film, only the α-Fe BCC phase was observed. For the following steps, experiments were conducted with the fabricated FePt alloy (see Figure 44). Alloying of Fe and Pt pellets was conducted in Istanbul Technical University with the help of Assoc. Prof. Dr. Cevat B. Derin. 20 nm of FePt thin film was deposited onto Si substrate. 5 nm of Cr was deposited as a cover layer. Sparkles were observed during the deposition. After that, the produced FePt thin-film was examined under XRD (see Figure 45).

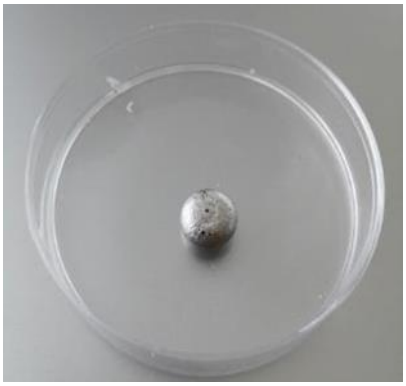

Figure 44 $Fe_{50}Pt_{50}$ alloy fabricated by arc melting

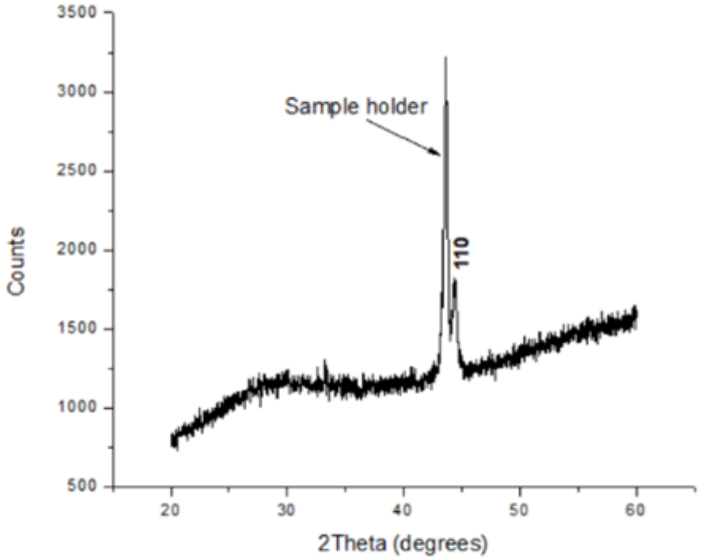

Figure 45 The XRD pattern of FePt thin film (20 nm)

In the XRD pattern, the α-Fe BCC phase was observed. Different melting temperatures resulted in an inhomogeneous deposition. Thus the composition of the thin film varies on different spots on the surface. Fe and Pt pellets were deposited separately in the following experiments. A deposition rate of [20.2nm Fe/17.4nm Pt] was tried as in the study published in the literature (Zotov, Feydt, & Ludwig, 2008). 20 nm Cr was deposited as a buffer and cover layers. The deposited FePt thin film then annealed at 300˚C, 350˚C, 500˚C, and 700˚C. Samples went under XRD and VSM experiments before and after annealing (see Figure 46 and Figure 47).

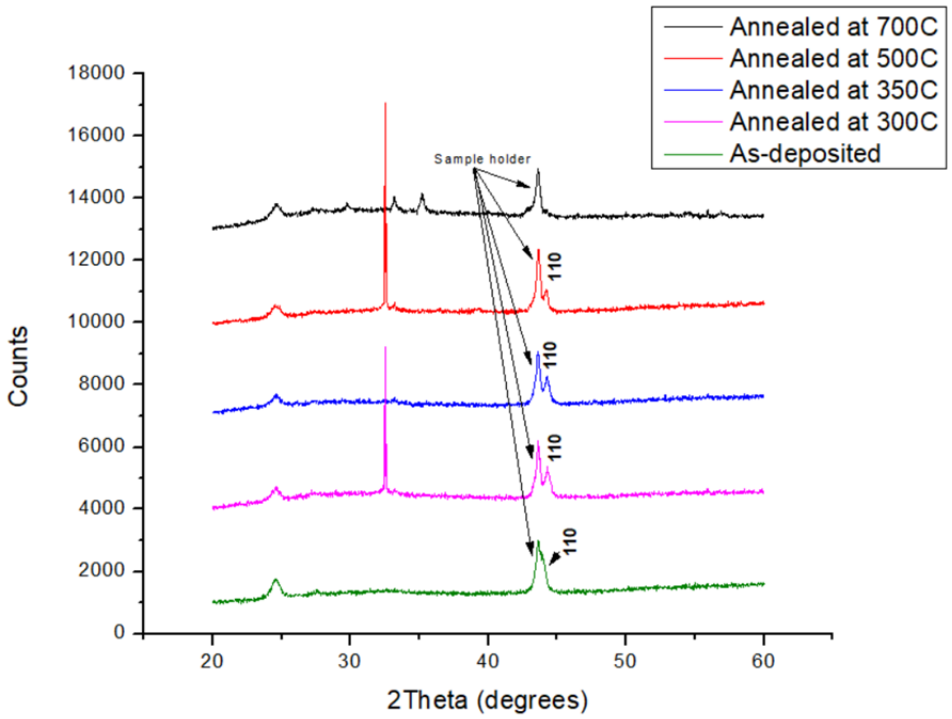

Figure 46 The XRD pattern of FePt thin film before and after annealing

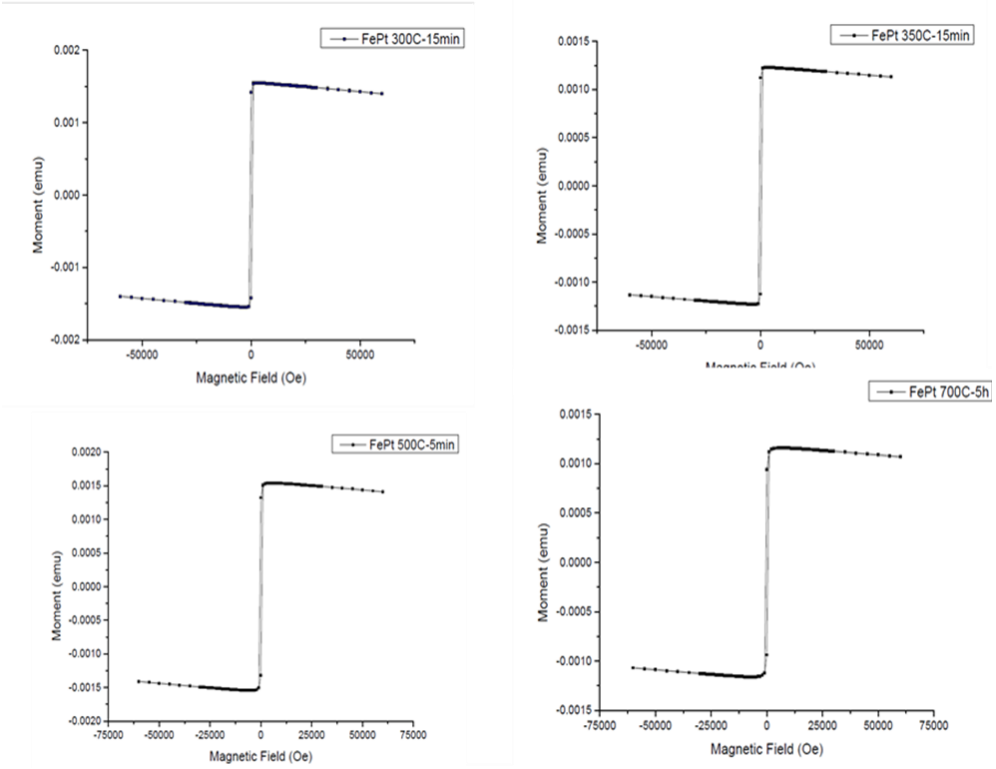

Figure 47 VSM measurements of annealed FePt thin films

Fabricated FePt thin film showed no peaks in the XRD pattern due to its amorphous structure before annealing. The α-Fe BCC phase was observed in the FePt thin films annealed at 300˚C, 350˚C, and 500˚C. Oxidation was observed in the thin film annealed at 700˚C. After VSM measurements, all hysteresis loops of the samples showed soft ferromagnetic properties as in properties of Fe. The sputtering method was decided to be used as the next step.

3.5. FePt Micromagnets Synthesized by Sputtering Technique

FePt thin films were synthesized to replace NdFeB magnets as an alternative magnet material. After the production procedure, characterization experiments were carried out. The experiments started with a For examining the phase and the structure of the samples, XRD measurements were studied. For examining the topography of the samples, SEM images were taken. The atomic composition of FePt micromagnets was calculated with EDS measurements. For magnetic properties, FePt samples were measured by VSM and VSM-SQUID techniques.

For comparison, the characteristic XRD pattern of FCT phase FePt is shown in Figure 48.

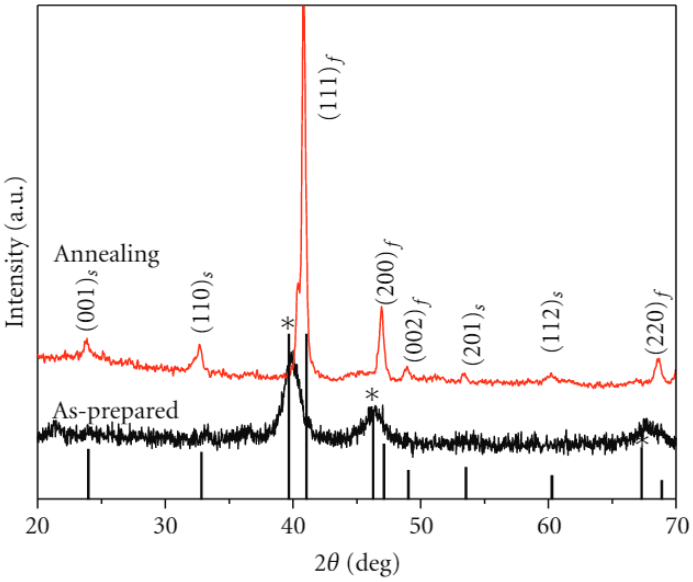

Figure 48 The characteristic XRD pattern of L10 ordered FCT FePt (Hoang Nam et al., 2012)

3.5.1. FePt Thin Films Synthesized by Using a Hybrid FePt Target (S1) by Sputtering Technique

Experiments were started with using the hybrid FePt target with 2-Pt pieces. The aim was to achieve an atomic composition of %50:50 Fe:Pt. The structures were deposited at 400°C temperature. The vacuum chamber was under a base pressure of 5 x 10^{-6} mbar. Sputtering was done under 30 mTorr of Ar gas atmosphere. A thickness of 50 nm of FePt thin film was deposited with an applied power of 59,67-Watts. A deposition rate of 0.8 Å/s was obtained with these parameters. The result of XRD measurement for produced FePt thin film is shown below (see Figure 49).

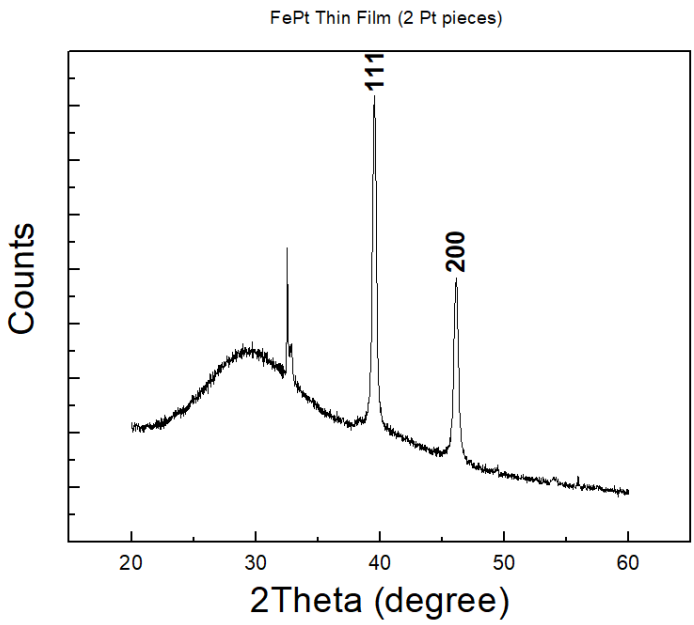

Figure 49 XRD pattern of S1 FePt thin film

From the XRD pattern of the sample, it can be said that produced FePt thin film showed an FCC phase with a composition of $Fe_{0.84}Pt_{0.16}$. The samples were then examined under SEM shown in Figure 50. In order to confirm the composition, elemental analysis measurement was conducted by EDS (see Figure 51).

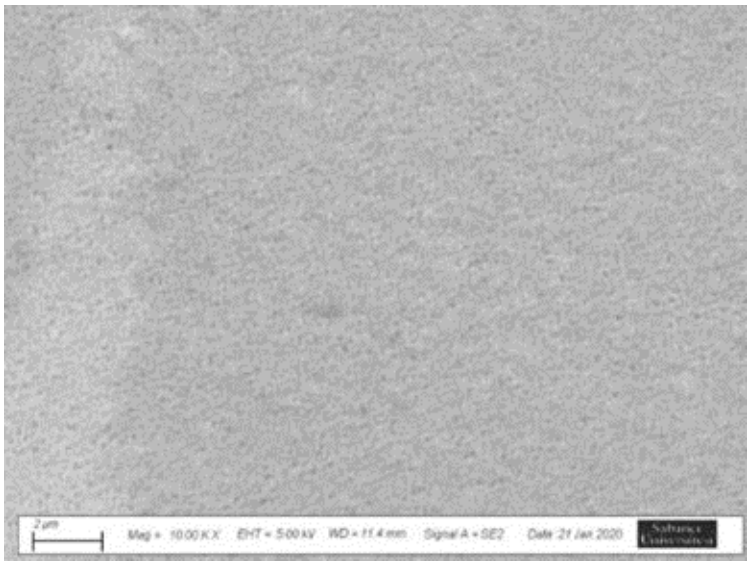

Figure 50 SEM image of FePt thin film synthesized using a hybrid FePt target with 2-Pt pieces

Element	At. No.	Netto	Mass [%]	Mass Norm. [%]	Atom [%]	abs. error [%] (1 sigma)	rel. error [%] (1 sigma)
Platinum	78	36452	18.81	42.83	17.66	0.75	3.98
Iron	26	11334	25.11	57.17	82.34	0.93	3.71
		Sum	**43.92**	**100.00**	**100.00**		

Figure 51 Elemental analysis for FePt sample (hybrid FePt target 2 Pt pieces)

It can be stated that the sputtered FePt thin film was not homogeneously distributed, resulting in contrast in the SEM image. Furthermore, from the elemental analysis of the sample, the atomic composition was confirmed to be ~82:18 Fe:Pt. With these results, it was decided to continue the experiments with a target with more Pt pieces to achieve an atomic composition of %50:50.

3.5.2. FePt Thin Films Synthesized by Using a Hybrid FePt Target (S2) by Sputtering Technique

At first, the third Pt piece was mounted to the FePt target. Then the sputtering experiment was carried out. The Structures were deposited at first at 400°C. The vacuum chamber was under base pressure of 5 x 10-6 mbar. Sputtering was done under 20 mTorr of Ar gas. Cr (99.99%) buffer and cover layers with thicknesses 5 nm and 15 nm, respectively, were deposited onto Si substrate. A power of 49-Watts was applied on Cr, resulting in a deposition rate of 0.6 Å/s. A thickness of 100 nm of FePt thin film was deposited with an applied power of 53-Watt and a deposition rate of 1.7 Å/s in between the Cr layers. After the deposition, samples were annealed under Ar/H2 (%5) gas at 500°C, 600°C, 650°C, and 700°C for 2 hours in order to find the optimum annealing temperature (see Figure 52). A new set of samples were then produced with the same parameters except for the deposition temperature. The second set was deposited at room temperature. After the deposition, they were annealed at the optimum temperature for 2, 4, and 6 hours in order to find the optimum annealing time (see Figure 53). Then, the sample was examined under XRD in order to see the phase of the sample. Elemental analysis of the samples was calculated by EDS (see Figure 54). Magnetic properties were measured under VSM (see Figure 55).

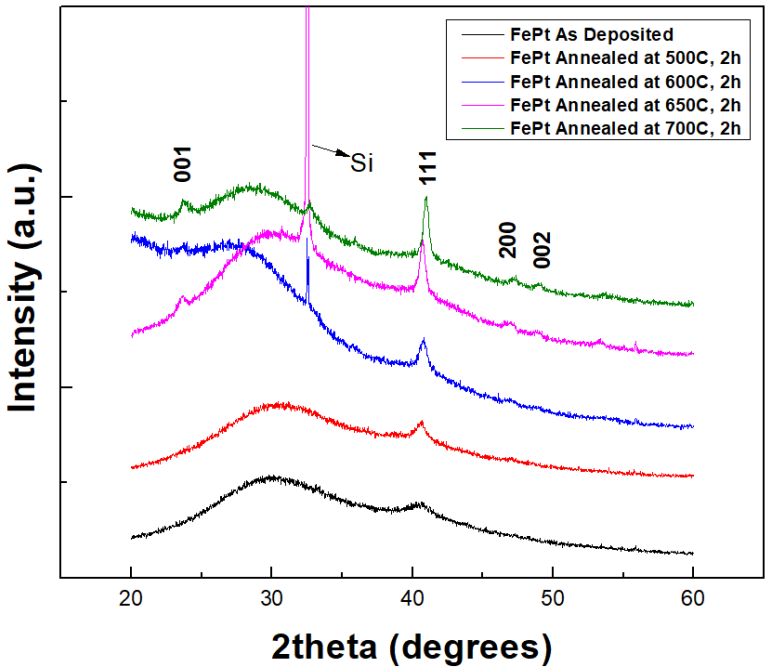

Figure 52 XRD patterns of S2 FePt thin films at different annealing temperatures

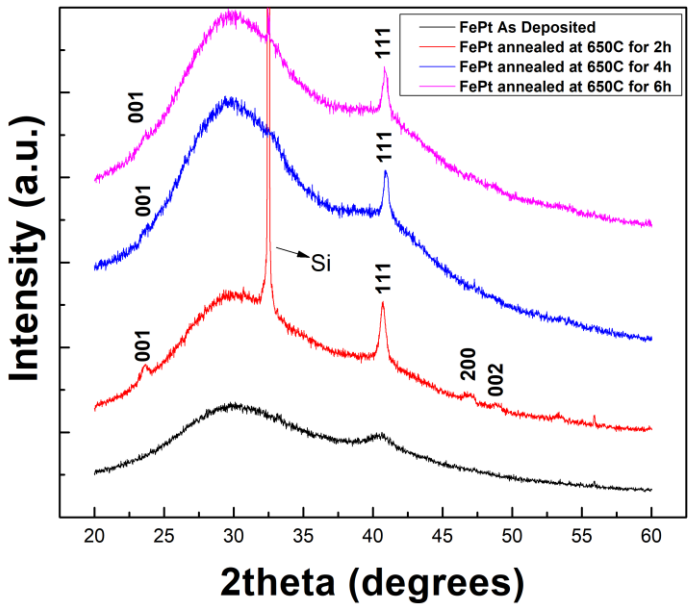

Figure 53 XRD patterns of S2 FePt thin films for different annealing times

Element	At. No.	Netto	Mass [%]	Mass Norm. [%]	Atom [%]	abs. error [%] (1 sigma)	rel. error [%] (1 sigma)
Chromium	24	5153	0.00	0.00	0.00	0.00	0.86
Iron	26	7777	5.45	38.00	68.16	0.20	3.67
Platinum	78	22625	8.89	62.00	31.84	0.37	4.20

Figure 54 Elemental analysis of S2 FePt thin films measured by EDS

By examining the peak intensities, the optimum annealing temperature was set to 650°C. Also, it can be stated after examining the XRD results from Figure 52 that while the as-deposited FePt thin film showed the characteristic peaks for the FCC phase, it transformed into the FCT phase of Iron (III) Platinum, Fe_3Pt, after annealing. The elemental analysis from Figure 54 confirms the resulted composition from the XRD results. The S2 FePt thin films showed ~62:38% (at.) composition. Compared with the XRD results of S1 FePt thin film, S2 FePt thin film is closer to the desired atomic composition. Between the two experiments, the latter is found to be closer to the desired structure but was not sufficient as 50:50% (at.) Fe:Pt. Then, the experiments were carried on with the hybrid FePt target with 4 Pt pieces, S3.

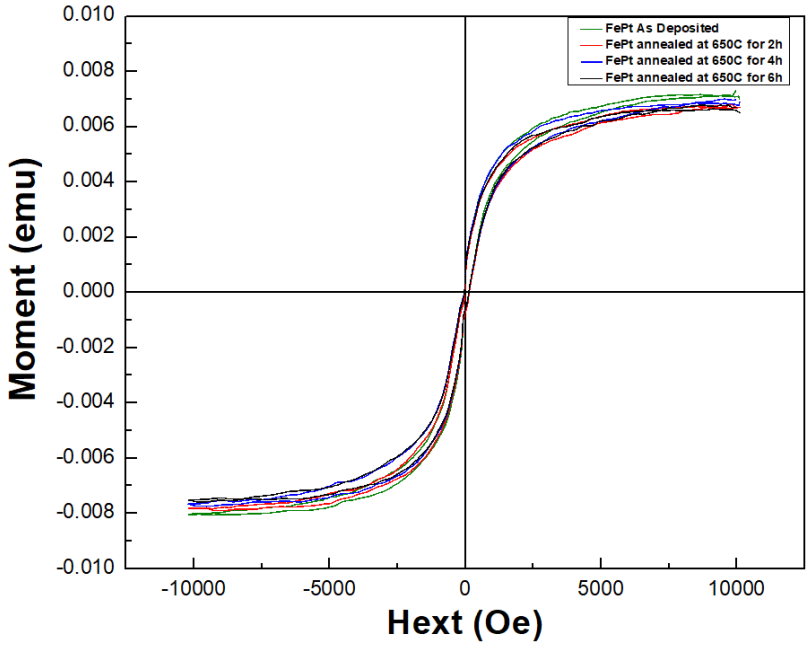

Figure 55 Hysteresis loops of S2 FePt thin films measured by VSM

The hysteresis loop of S2 FePt thin films showed soft magnetic properties after an applied an external field with a range from -10 kOe to 10 kOe. The coercivity values obtained from the VSM measurement for S2 FePt thin films before the annealing and annealed at 650°C for 2, 4, and 6 hours were 103.89, 97.55, 71.25, and 99.21 Oe, respectively. The desired 50:50% (at.) composition could not be achieved with S2 FePt thin films. The experiments continued with a FePt target that had a higher Pt ratio.

3.5.3. FePt Thin Films Synthesized by Using a Hybrid FePt Target (S3) by Sputtering Technique

A new hybrid FePt target with a mounted 4-Pt piece on the race track of the target was developed. The target was used in sputtering experiments. Parameters of the sputtering experiments were the same as previous. The Structures were deposited at room temperature. The vacuum chamber was under base pressure of 5 x 10-6 mbar. Sputtering was done under 20 mTorr of Ar gas. Cr (99.99%) buffer and cover layers with thicknesses 15 nm and 5 nm, respectively, were deposited onto (100) Si substrate. A power of 48.75-Watts was applied on Cr, resulting in a deposition rate of 0.6 Å/s. A thickness of 100 nm of FePt thin film was deposited with an applied power of 53.25-Watt and a deposition rate of 1.8 Å/s in between the Cr layers. After the deposition, samples were annealed under Ar/H2 (%5) gas at 650°C for 2, 4, and 6 hours. The samples (S3) were then examined under XRD in order to see the phase of the sample shown in Figure 56. Elemental analysis of the samples was calculated by EDS to measure the composition of the deposited thin film (see Figure 57). Magnetic properties were then measured under VSM and VSM-SQUID(see Figure 58 and Figure 59).

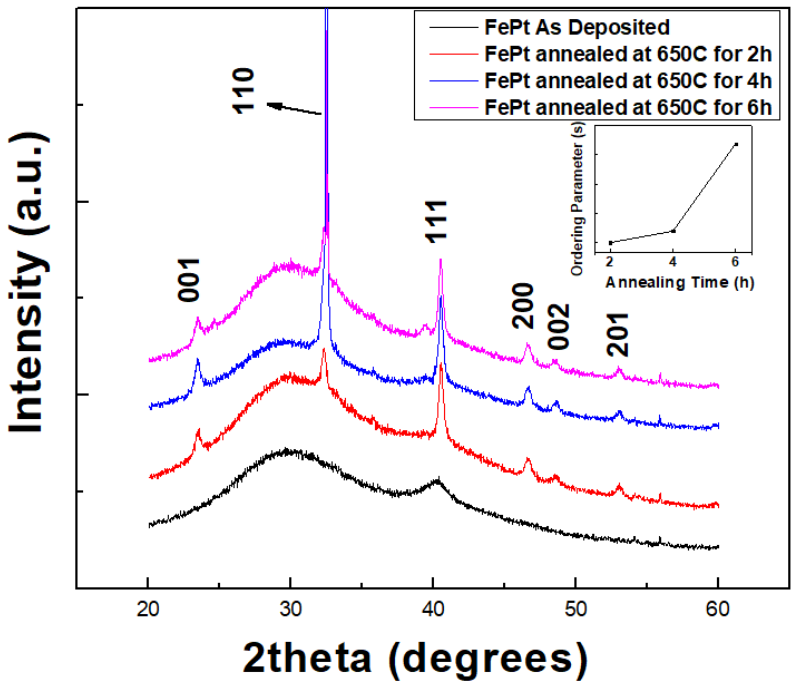

Figure 56 XRD patterns of S3 FePt thin films annealed for different annealing temperatures. Inlet: ordering parameter versus annealing time

Element	At. No.	Netto	Mass [%]	Mass Norm. [%]	Atom [%]	abs. error [%] (1 sigma)	rel. error [%] (1 sigma)
Iron	26	7877	4.77	25.71	54.73	0.18	3.73
Platinum	78	45017	13.80	74.29	45.27	0.56	4.05
		Sum	**18.57**	**100.00**	**100.00**		

Figure 57 Elemental analysis of S3 FePt thin films measured by EDS

After varying the annealing temperatures from 2 hours to 6 hours, the optimum annealing time was set to a minimum of 4 hours. As shown in Figure 56, the transition of the structure from FCC to FCT was observed in the XRD pattern after annealing, showing that the atomic composition of FePt is obtained as desired. The elemental analysis for the S3 FePt thin film samples showed an atomic ratio of ~55:45% (at.) Fe:Pt, confirming the XRD results. The XRD patterns of the S3 FePt thin film corresponded to the characteristic diffraction peaks of the $L1_0$ ordered FCT phase FePt, which is the desired structure. In order to examine the chemical ordering for FePt thin films, the chemical ordering parameter, S, was calculated according to the following formula (Rong et al., 2006),

$$S \cong 0.85\left[\frac{I_{001}}{I_{111}}\right]^{1/2} \qquad (3.1)$$

where I_{001} and I_{111} are the measured intensities of the superlattice and the fundamental peaks. As expected, S increases by increasing the annealing time, reaching a maximum value of ~0.7 (see Figure 56 inlet).

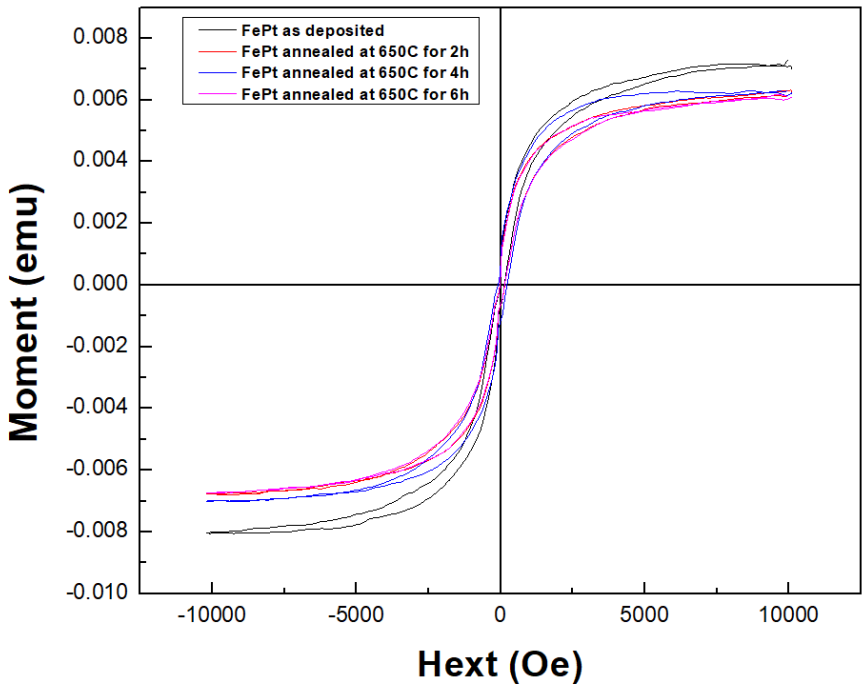

Figure 58 Hysteresis loops of S3 FePt thin films measured by VSM

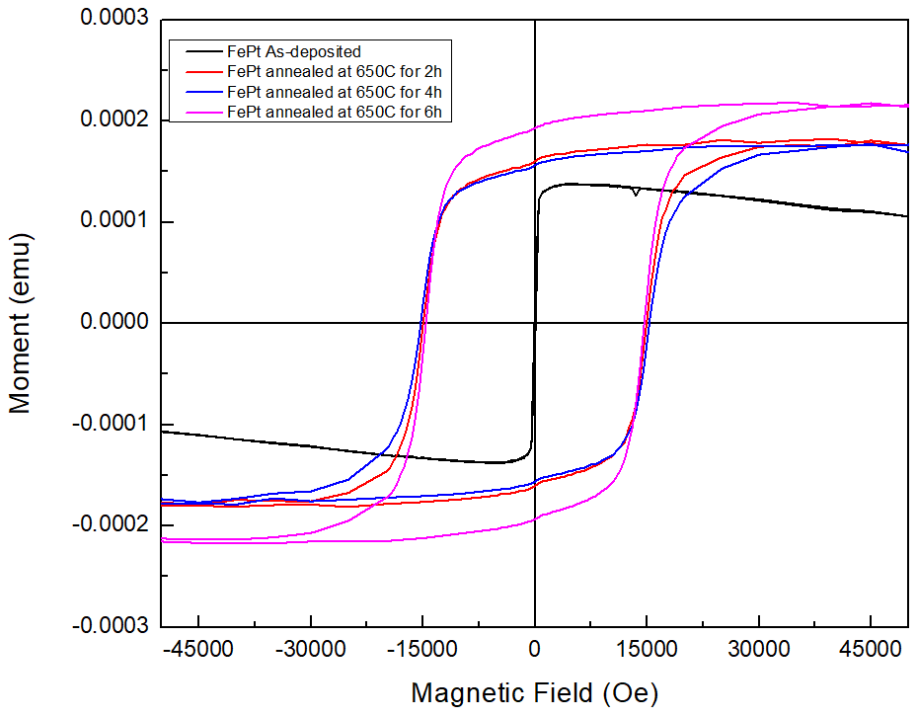

Figure 59 Hysteresis loops of S3 FePt thin films measured by VSM-SQUID

After the VSM measurements for S3 FePt thin films before and after the annealing, it resulted in the same as S2 FePt thin film samples. The range of the applied external field was from -10 kOe to 10 kOe. It showed soft magnetic properties as a result. However, these results were found to be unreliable since the VSM instrument was not able to sense the moment of the samples. Thus, the magnetic properties were then measured by VSM-SQUID, which is more sensitive. High coercivity values, approximately 15 kOe, were obtained from the SQUID results showing hard ferromagnetic properties. The saturation magnetization values before annealing and after the 2, 4, and 6 hours of annealing were measured as 153 emu/cm^3, 201 emu/cm^3, 196 emu/cm^3, and 242 emu/cm^3, respectively. After measuring the magnetic properties, it can be said that continuous FePt thin films with the right composition and phase were successfully synthesized. As a next step, the FePt target with 4 Pt pellets was used for the synthesis of FePt micro-magnets and an undulator prototype.

3.5.4. Building An Undulator Prototype Synthesized with FePt Micromagnets

After synthesizing FePt micromagnets successfully, an undulator prototype was built with FePt micromagnets. The undulator design was transferred onto the Si substrate by the photolithography technique. During the sample preparation, a 7µm thick resist was obtained with the parameters for the spin-coating step given in the previous chapter. Figure 60 shows the light microscopy image of as-deposited FePt micromagnets fabricated onto (100) Si wafer substrate by lithography. An undulator pattern with its period ranging from 250 µm to 10 mm was successfully fabricated. After lithography, FePt thin film was deposited onto the design by sputtering with the same parameters. The produced samples were annealed at 750°C under Ar/H_2 atmosphere for 2, 4, and 6 h, respectively. The samples were then examined under XRD in order to see the phase of the sample shown in Figure 61. Elemental analysis of the samples was calculated by EDS to measure the composition of the micro magnets (see Figure 62). Magnetic properties were then measured under VSM-SQUID(see Figure 63). The surface topography of the samples also was examined under SEM shown in Figure 64, Figure 65, and Figure 66.

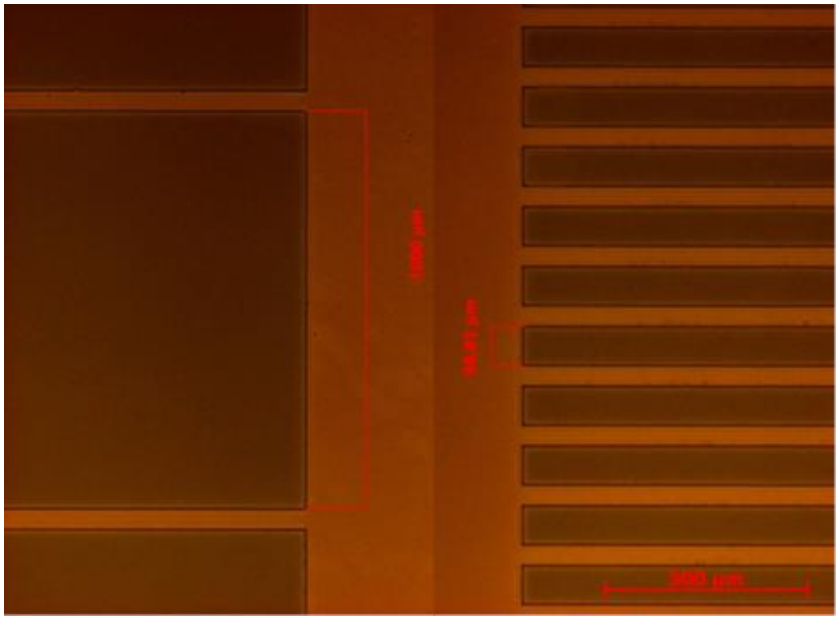

Figure 60 Light microscope image of two separate deposited undulator sections. Micromagnets have 1 mm (left) and 100 µm (right) in width

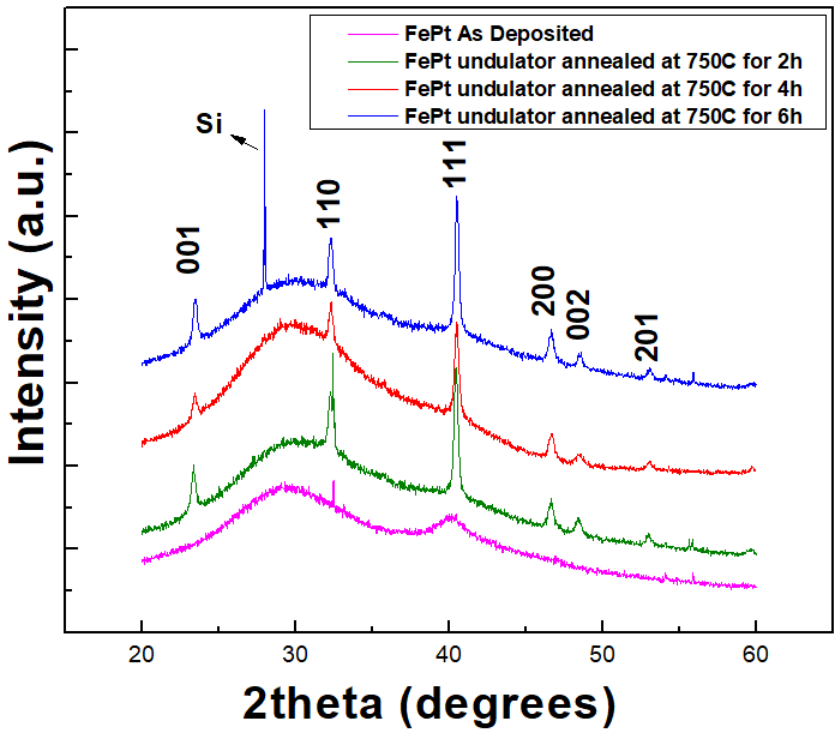

Figure 61 XRD patterns of FePt undulator prototype as-deposited (pink), annealed at 750°C for 2h (green), 4h (red), and 6h (blue)

Element	At. No.	Netto	Mass [%]	Mass Norm. [%]	Atom [%]	abs. error [%] (1 sigma)	rel. error [%] (1 sigma)
Iron	26	1440	4.49	25.68	54.69	0.21	4.78
Platinum	78	9222	12.99	74.32	45.31	0.55	4.26

Figure 62 Elemental analysis of the undulator prototype measured by EDS

The XRD patterns of the fabricated sample matched to the characteristic diffraction peaks of the $L1_0$ ordered FCT phase FePt after annealing under Ar/H_2 atmosphere at 750°C for 2, 4, and 6 hours, although the as-deposited FePt film was in the FCC structure, as it is shown in Figure 61. The elemental analysis also confirmed that the achieved composition is ~55:45 (at.)% Fe:Pt as it is desired, similar to the S3 FePt thin films.

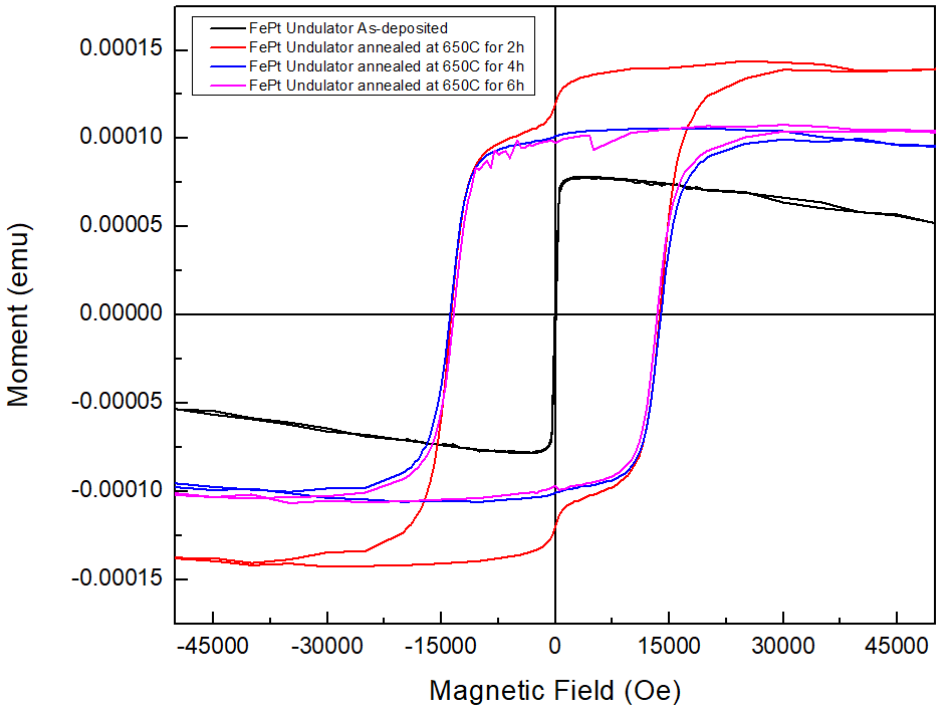

Figure 63 Hysteresis loops of the undulator prototype measured by VSM-SQUID

The VSM-SQUID measurements show that the produced designed microstructures showed hard ferromagnetic behavior. A high coercivity value of ~14 kOe was obtained. The saturation magnetization values before annealing and after the 2, 4, and 6 hours of annealing were measured as 87 emu/cm^3, 159 emu/cm^3, 117 emu/cm^3, and 119 emu/cm^3, respectively.

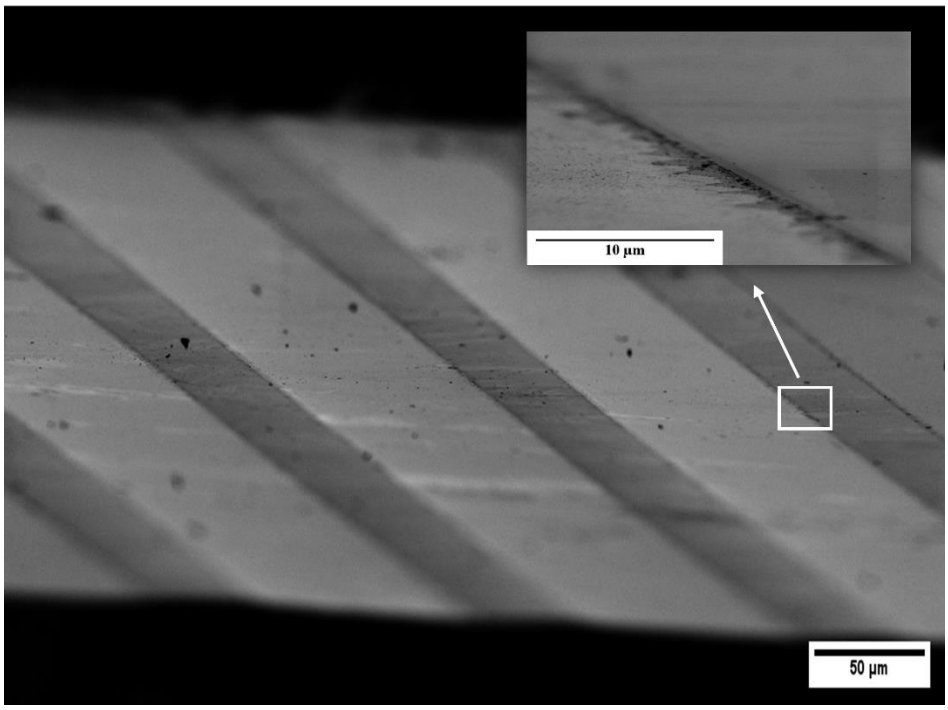

Figure 64 SEM image of FePt undulator prototype

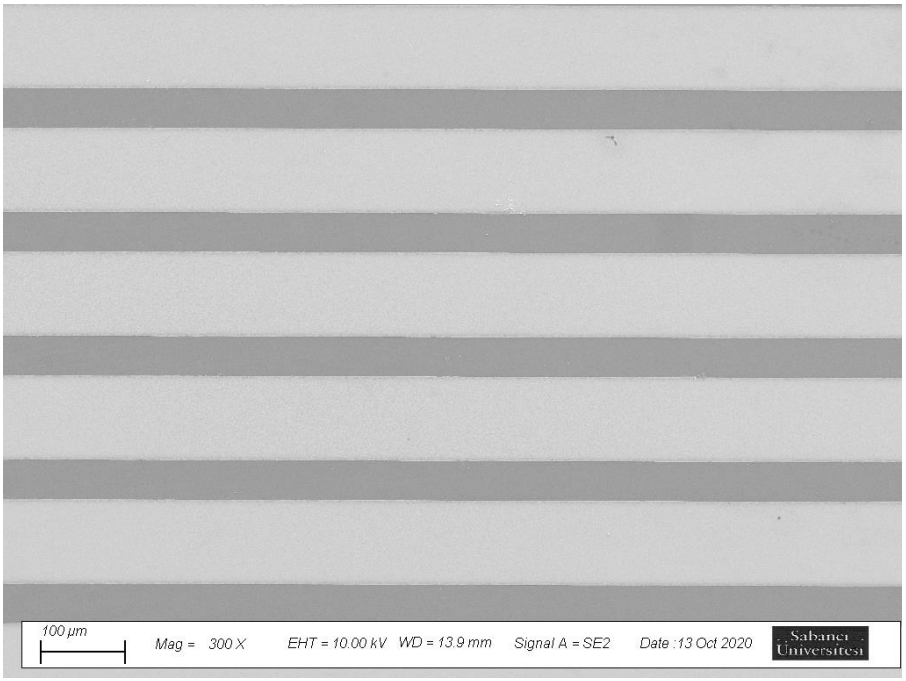

Figure 65 SEM image of a top view of the undulator prototype with 250 µm of undulator period

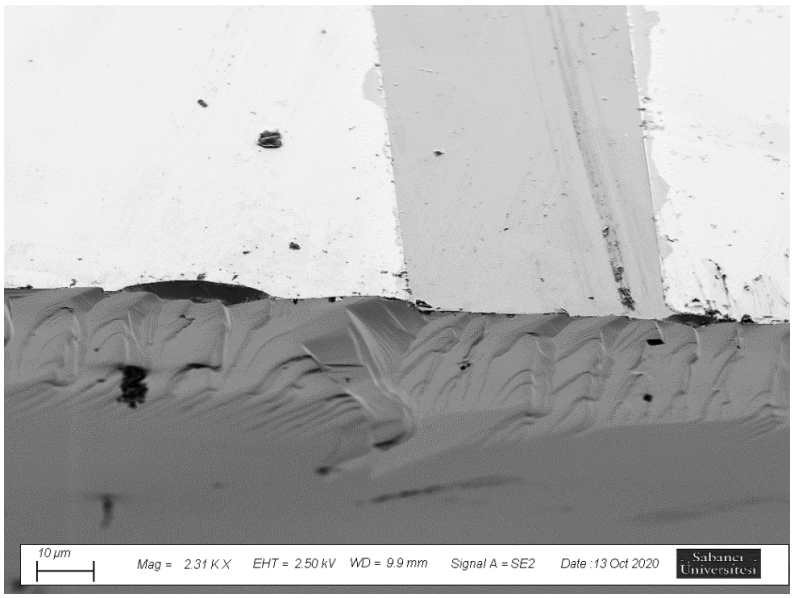

Figure 66 The cross-section SEM image of the undulator prototype

In the SEM images, the brighter structures represent the produced FePr micromagnets, while the darker spots represent the Si substrate. In addition, Scanning Electron Microscope (SEM) images of post-annealed FePt micromagnets showed no degradation. (Figure 64). The characterization of the samples indicated that fabricating hard ferromagnetic $L1_0$ ordered FCT phase FePt micromagnets was achieved successfully. Furthermore, the first step of building the sub-millimeter period undulator prototype was completed successfully.

3.5.5. Magnetizing FePt Micromagnets And Designing An Undulator Prototype

In this section, produced FePt micromagnets were magnetized alternatively by a pulse magnetizer connected to a CNC laser machine (see Figure 67). The prepared setup has parts that are able to move in -xyz directions. FePt micromagnets were stabilized at the stage of the CNC laser machine. Then, with the help of a pulse magnetizer, a magnetic flux is directed to the samples through an iron rod that had a tunneling purpose. After the initial applied magnetic flux, the target moved by the step motors to the following

structure. Then, the direction of the flux was changed to the opposite, and it was applied to the new structure. By this method, the FePt micromagnets were tried to be magnetized in an alternative manner. The samples were examined under Magnetic Force Microscopy to be able to control the direction of the magnetization. Then, by magnetizing the two sets of FePt micromagnets, an undulator prototype had been fabricated.

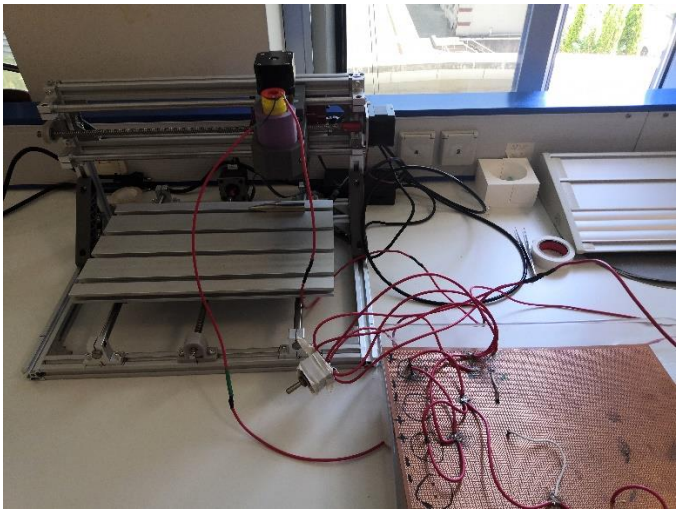

Figure 67 Experimental setup for magnetizing the FePt micromagnets

3.6. Future Work

A proper casing for the undulator prototype constructed by the commercialized N45 grade Nickel-plated 3 mm cubic NdFeB magnets mounted in different magnetic arrays could be fabricated in the future. A design that will allow adjusting the gap between the two sets of magnets will provide easier conditions for the trials of the undulator prototype with a varying gap between the magnets. Also, for mounting the NdFeB magnets in the Halbach array, epoxy adhesive glue can be used to hold the magnets together since the magnetic forces prevent the stabilization of the magnets.

An undulator prototype was fabricated successfully. However, testing the prototype can be researched in future projects. The performance of the fabricated prototype should be tested. TARLA will be conducting a simulation for testing the performance of the sub-millimeter period undulators consisted of FePt micromagnets. To be able to test the prototype physically, new studies should be carried out.

4. CONCLUSION

An undulator prototype was tried to be produced by micromachining a commercialized N52 grade NdFeB magnet. 1 mm thick NdFeB magnet slices had multiple microcracks and severe deformation on the surface after the micromachining procedure. Better results were obtained when the same procedure was applied with femtosecond lasers.

Commercialized NdFeB cube magnets were mounted with different magnetic arrays to produce an undulator prototype. Halbach and Up-Down magnetic array were obtained. Their magnetic field map was measured with a scanning hall probe. The experimental results confirmed the values obtained from simulations that were released to the scientific literature.

A hybrid FePt target with Fe base and 4 Pt pieces was developed to be able to synthesize Fe:Pt thin films with ~55:45% (at.) composition. FePt thin films were synthesized by magnetron sputtering. Synthesized FePt thin films were annealed under Ar/H2 at 650°C and 750°C for 2, 4, and 6h, and phase transformation from FCC to FCT was observed. After VSM-SQUID measurements, high coercivity, ~15 kOe, was obtained. An undulator pattern consisted of FCT $L0_1$ phase FePt micromagnets was produced.

The first sub-mm undulator prototype with a period ranging from 250 μm to 10 mm was successfully synthesized using $L1_0$ ordered FePt micro magnets. This advancement will open the door for the next generation of small-scale FEL's.

5. REFERENCES

Akdogan, N. G., & Akdogan, O. (2019). Synthesis of Nd-Fe-B/Fe hybrid micro-magnets. *AIP Advances*, *9*(12). https://doi.org/10.1063/1.5130412

Akdogan, N. G., Polat, O., & Akdogan, O. (2020). Magnetic field mapping simulations of sub-mm period undulators for the next generation X-ray free electron lasers. *Nuclear Instruments and Methods in Physics Research, Section A: Accelerators, Spectrometers, Detectors and Associated Equipment*, *969*(March), 164062. https://doi.org/10.1016/j.nima.2020.164062

Akdogan, Nilay G., Li, W., & Hadjipanayis, G. C. (2011). Anisotropic Nd2Fe14B nanoparticles and nanoflakes by surfactant-assisted ball milling. *Journal of Applied Physics*, *109*(7), 2009–2012. https://doi.org/10.1063/1.3567049

Akdogan, Nilay G, Hadjipanayis, G. C., & Sellmyer, D. J. (2010). Novel Nd 2 Fe 14 B nanoflakes and nanoparticles for the development of high energy nanocomposite magnets. *Nanotechnology*, *21*(29), 295705. https://doi.org/10.1088/0957-4484/21/29/295705

Arora, A. (2018). Optical and electric field control of magnetism. *University of Potsdam*, 11–20.

Baruwati, B. (2015). *Studies on the Synthesis, Characterization, Surface Modification and Application of Nanocrystalline Nickel Ferrite*. (April). Retrieved from https://www.researchgate.net/publication/49177963

Bian, B., Laughlin, D. E., Sato, K., & Hirotsu, Y. (2000). Fabrication and nanostructure of oriented FePt particles. *Journal of Applied Physics*, *87*(9 III), 6962–6964. https://doi.org/10.1063/1.372900

Blewett, J. P. (1998). Synchrotron radiation - Early history. *Journal of Synchrotron Radiation*, *5*(3), 135–139. https://doi.org/10.1107/S0909049597043306

Budde, M., Lüpke, G., Parks Cheney, C., Tolk, N. H., & Feldman, L. C. (2000). Vibrational lifetime of bond-center hydrogen in crystalline silicon. *Physical Review Letters*, *85*(7), 1452–1455. https://doi.org/10.1103/PhysRevLett.85.1452

Coffey, K. R., Parker, M. A., & Howard, J. K. (1995). High Anisotropy L10 Thin Films

for Longitudinal Recording. *IEEE Transactions on Magnetics*, *31*(6), 2737–2739. https://doi.org/10.1109/20.490108

Edwards, G., Logan, R., Copeland, M., Reinisch, L., Davidson, J., Johnson, B., … O'Day, D. (1994). Tissue ablation by a free-electron laser tuned to the amide II band. *Nature*, *371*(6496), 416–419. https://doi.org/10.1038/371416a0

Einstein, A. (1917). On the Quantum Theory of Radiation (translation). In *Physik. Z.* (Vol. 18). Retrieved from https://link.aps.org/doi/10.1103/RevModPhys.51.863

Goldstein, J. I., Newbury, D. E., Michael, J. R., Ritchie, N. W. M., Scott, J. H. J., & Joy, D. C. (2018). Scanning Electron Microscopy and X-Ray Microanalysis. In *Microscopy and Microanalysis* (Vol. 24). https://doi.org/10.1007/978-1-4939-6676-9

Gutfleisch, O., Lyubina, J., Müller, K. H., & Schultz, L. (2005). FePt hard magnets. *Advanced Engineering Materials*, *7*(4), 208–212. https://doi.org/10.1002/adem.200400183

Hoang Nam, N., Thi Thanh Van, N., Dang Phu, N., Thi Hong, T., Hoang Hai, N., & Luong, N. H. (2012). Magnetic properties of FePt nanoparticles prepared by sonoelectrodeposition. *Journal of Nanomaterials*, *2012*. https://doi.org/10.1155/2012/801240

Joos, K. M., Shen, J. H., Shetlar, D. J., & Casagrande, V. A. (2000). Optic nerve sheath fenestration with a novel wavelength produced by the free electron laser (FEL). *Lasers in Surgery and Medicine*, *27*(3), 191–205. https://doi.org/10.1002/1096-9101(2000)27:3<191::AID-LSM1>3.0.CO;2-D

Kelly, P. ., & Arnell, R. . (2000). Magnetron sputtering: a review of recent developments and applications. *Vacuum*, *56*(3), 159–172. https://doi.org/10.1016/S0042-207X(99)00189-X

Madey, J. M. J. (1971). Stimulated emission of bremsstrahlung in a periodic magnetic field. *Journal of Applied Physics*, *42*(5), 1906–1913. https://doi.org/10.1063/1.1660466

Motz, H. (1951). Applications of the radiation from fast electron beams. *Journal of Applied Physics*, *22*(5), 527–535. https://doi.org/10.1063/1.1700002

Motz, H., Thon, W., & Whitehurst, R. N. (1953). Experiments on radiation by fast electron beams. *Journal of Applied Physics*, *24*(7), 826–833. https://doi.org/10.1063/1.1721389

Nisticò, R., Cesano, F., & Garello, F. (2020). Magnetic materials and systems: Domain structure visualization and other characterization techniques for the application in the materials science and biomedicine. In *Inorganics* (Vol. 8). https://doi.org/10.3390/inorganics8010006

Oshida, Y. (2013). Advanced Materials, Technologies, and Processes. In *Bioscience and Bioengineering of Titanium Materials* (pp. 457–497). https://doi.org/10.1016/B978-0-444-62625-7.00012-1

Pauli, W. (1925). Über den Zusammenhang des Abschlusses der Elektronengruppen im Atom mit der Komplexstruktur der Spektren. *Zeitschrift Für Physik*, *31*(1), 765–783. https://doi.org/10.1007/BF02980631

Pellegrini, C., Marinelli, A., & Reiche, S. (2016). The physics of x-ray free-electron lasers. *Reviews of Modern Physics*, *88*(1), 1–55. https://doi.org/10.1103/RevModPhys.88.015006

Qiu, Z. Y., Chen, C., Wang, X. M., & Lee, I. S. (2014). Advances in the surface modification techniques of bone-related implants for last 10 years. *Regenerative Biomaterials*, *1*(1), 67–79. https://doi.org/10.1093/rb/rbu007

Rong, C. B., Li, D., Nandwana, V., Poudyal, N., Ding, Y., Wang, Z. L., … Liu, J. P. (2006). Size-dependent chemical and magnetic ordering in L10-FePt nanoparticles. *Advanced Materials*, *18*(22), 2984–2988. https://doi.org/10.1002/adma.200601904

Salah, N., Habib, Khan, Memic, Azam, Al-Hamedi, … Habib. (2011). High-energy ball milling technique for ZnO nanoparticles as antibacterial material. *International Journal of Nanomedicine*, 863. https://doi.org/10.2147/IJN.S18267

Schneidmiller, E. A., & Yurkov, M. V. (2011). Photon beam properties at the European XFEL. *Xfel.Eu Tr-2011-006*, (December 2010). Retrieved from https://www.xfel.eu/sites/sites_custom/site_xfel/content/e35165/e46561/e46886/e46963/e46964/xfel_file46967/TR-2011-006_Photon_Beam_Properties_eng.pdf

Shintake, T. (2007). *SASE-FEL MACHINE*. 89–93.

Suryanarayana, C. (2001). Mechanical alloying and milling. *Progress in Materials Science*, *46*(1–2), 1–184. https://doi.org/10.1016/S0079-6425(99)00010-9

Thomas, E. L., Millican, J. N., Okudzeto, E. K., & Chan, J. Y. (2006). Crystal Growth and the Search for Highly Correlated Intermetallics. *Comments on Inorganic Chemistry*, *27*(1–2), 1–39. https://doi.org/10.1080/02603590600666215

Vinet, L., & Zhedanov, A. (2011). A 'missing' family of classical orthogonal polynomials. *Journal of Physics A: Mathematical and Theoretical*, *44*(8), 085201. https://doi.org/10.1088/1751-8113/44/8/085201

W. H. Bragg, W. L. B. (1913). The reflection of X-rays by crystals. *Proceedings of the Royal Society of London. Series A, Containing Papers of a Mathematical and Physical Character*, *88*(605), 428–438. https://doi.org/10.1098/rspa.1913.0040

Weller, D., Moser, A., Folks, L., Best, M. E., Lee, W., Toney, M. F., & Schwickert, M. (2000). High ku materials approach to 100 gbits/in2. *IEEE Transactions on Magnetics*, *36*(1 PART 1), 10–15. https://doi.org/10.1109/20.824418

Yu, J., Ruediger, U., Kent, A. D., Farrow, R. F. C., Marks, R. F., Weller, D., … Parkin, S. S. P. (2000). Magnetotransport and magnetic properties of molecular-beam epitaxy L10 FePt thin films. *Journal of Applied Physics*, *87*(9 III), 6854–6856. https://doi.org/10.1063/1.372864

Zotov, N., Feydt, J., & Ludwig, A. (2008). Dependence of grain sizes and microstrains on annealing temperature in Fe/Pt multilayers and L10 FePt thin films. *Thin Solid Films*, *517*(2), 531–537. https://doi.org/10.1016/j.tsf.2008.06.062